

# Efficient all-electron Bethe-Salpeter implementation using crystal symmetries

Jörn Stöhler,<sup>1,2</sup> Stefan Blügel,<sup>1,2</sup> and Christoph Friedrich<sup>2,\*</sup>

<sup>1</sup>*Institute for Theoretical Physics, RWTH Aachen University, 52056 Aachen, Germany*

<sup>2</sup>*Peter Grünberg Institut, Forschungszentrum Jülich and JARA, 52425 Jülich, Germany*

(Dated: March 27, 2026)

We describe an all-electron implementation of the Bethe-Salpeter equation (BSE) for the calculation of optical absorption spectra in the full-potential linearized augmented-plane-wave (FLAPW) method. So far, FLAPW implementations have resorted to a simple plane-wave basis for the bare and screened Coulomb potentials, thereby forgoing the all-electron description to some extent. In contrast, we expand the interaction potentials in the all-electron mixed basis. As in most implementations, the BSE is solved by the diagonalization of a two-particle Hamiltonian matrix, whose dimension is proportional to the number of  $\mathbf{k}$  points. Due to the large number of  $\mathbf{k}$  points required to converge the BSE, the resulting matrix becomes large even for small unit cells. We describe a method that exploits the crystal symmetries to accelerate the construction and diagonalization of the two-particle Hamiltonian. In particular, we employ group theoretical tools to bring the Hamiltonian into block-diagonal form. Furthermore, it is shown that often only one of the blocks needs to be taken into account for the optical absorption spectrum leading to a considerable speedup of the diagonalization step. The code allows for the inclusion of spin-orbit coupling and is parallelized with the possibility of storing the Hamiltonian in distributed memory over many nodes, keeping the memory demands low. To validate our implementation, we show optical absorption spectra and report exciton binding energies for bulk Si, LiF, and MoS<sub>2</sub>. By exploiting the crystal symmetries, we can reduce the dimension of the Hamiltonian matrix of Si by a factor of five, resulting in a 125-fold speedup in its diagonalization. The calculated spectra agree with available theoretical and experimental spectra from the literature. The calculated exciton binding energies of 22 meV and 76 meV for Si and MoS<sub>2</sub> are closer to experimental values than in previous BSE studies.

## I. INTRODUCTION

The Bethe-Salpeter equation (BSE) [1–4] enables the accurate computation of optical absorption spectra, electron energy-loss spectra, and exciton binding energies from first principles. It provides a unified description of the response of the interacting many-electron system to the electric field of photons or beam of electrons, treating plasmonic and excitonic excitations on the same footing. Diagrammatically, the former are described by a summation of Green-function bubbles and the latter by a summation of ladder diagrams to all orders. The BSE also incorporates all possible mixtures of the diagrams, which leads to a mutual renormalization of excitons and plasmons.

To date, most implementations of the BSE for periodic systems rely on a plane-wave [5–7] (or Gaussian [8]) basis with a pseudopotential approximation for the Kohn-Sham effective potential. In such an implementation, only the valence electrons are treated explicitly, whereas the contribution of the core electrons to the effective potential is approximated and fixed by the chosen pseudopotential. Furthermore, due to the smoothed form of the potential, the valence wavefunctions are pseudized close to the atomic nuclei, where they miss the rapid variations of the true energy eigenstates. Likewise, high-lying empty states, relevant for the construction of the screened interaction, differ substantially from true energy eigenstates because the pseudopotential approximation is made to work well only for the valence states, while it gets less accurate for high-lying states [9].

Full all-electron implementations of the BSE for periodic systems are scarce. Implementations based on the LAPW basis set [10–12] and on the linearized muffin-tin orbitals (LMTO) basis set [13] have been reported. More recently, an implementation of the BSE based on numerical atomic orbitals has also been introduced [14]. Both implementations based on the LAPW basis deviate from a full all-electron description, however, in that they project the (bare and screened) interaction potentials onto an auxiliary plane-wave basis, which cannot resolve the rapid variations close to the atomic nuclei. In our implementation, we do not resort to a plane-wave basis but expand all quantities in the LAPW basis and (in the case of the interaction potentials) its related mixed basis [15–17].

In a common approach, one reformulates the BSE as an eigenvalue problem with an effective electron-hole Hamiltonian. This Hamiltonian is represented in a basis of electron-hole wavefunction products. In periodic systems, typically a large number of  $\mathbf{k}$  points is required to converge the results, which makes the construction and diagonalization of the dense Hamiltonian matrix computationally expensive even for small systems. A possibility to reduce the computational cost without sacrificing accuracy is by exploiting crystal symmetries. For example, it is possible to restrict the  $\mathbf{k}$  points to an irreducible wedge of the Brillouin zone, which is routine in density-functional theory (DFT) codes. It is also possible in implementations of hybrid functionals [18] and the GW approximation [16], where an additional extended irreducible wedge has to be introduced because of nested  $\mathbf{k}$  summations.

Here, we describe our use of crystal and time-reversal symmetries to reduce the cost of BSE calculations. First, we speed up the construction of the two-particle Hamiltonian. We reduce the number of entries that need to be calculated explicitly, and calculate the rest by applying suitable symmetry transformations. Second, we bring the large and dense Hamiltonian into a block-diagonal form by a transformation to a symmetry-adapted basis. Often, only one of the blocks contributes to the spectrum. This significantly accelerates the diagonalization of the Hamiltonian, which is the most time-consuming part of the BSE calculation for large systems (or calculations with large  $\mathbf{k}$  grids).

We would like to emphasize that the symmetry-accelerated construction of the Hamiltonian and its transformation to the symmetry-adapted basis are exact. The computational speedup does not come at the expense of accuracy. (The smaller matrix size may even help reduce numerical rounding errors.) This stands in contrast to other techniques such as double-grid methods [3, 19], which necessarily introduce approximations. The approaches are, of course, compatible and can be combined.

In Sec. II, we briefly revisit the BSE in its formulation as an eigenvalue problem. We discuss our choice of basis sets, the LAPW and mixed basis in Sec. III. Then, we describe our implementation in the all-electron code SPEX [16], in particular the use of crystal symmetries in constructing and diagonalizing the electron-hole Hamiltonian. SPEX is part of the FLEUR family of codes [20]. In Sec. IV, we present illustrative results for Si, LiF, and bulk MoS<sub>2</sub> and compare them with the literature. The usage of crystal symmetries significantly speeds up the computations, as illustrated by a BSE solution of Si on a very dense 60×60×60  $\mathbf{k}$ -point grid. The transformation to a symmetry-adapted product basis using group theory results in a performance increase by a factor of 125 for the diagonalization step in the case of Si. Section V concludes the paper with a summary of the main results. The BSE implementation based on group theory has previously been described in Ref. 21, the master's thesis of the first author.

## II. THEORY

Theoretical optical absorption spectra of solids are given by the imaginary part of the macroscopic electronic dielectric function  $\varepsilon_M(\omega)$ , which is related to the inverse microscopic electronic dielectric function by [22, 23]

$$\varepsilon_M(\omega) = \lim_{\mathbf{q} \rightarrow \mathbf{0}} \frac{1}{\varepsilon_{\mathbf{0}\mathbf{0}}^{-1}(\mathbf{q}, \omega)} \quad (1)$$

with the plane-wave representation

$$\varepsilon_{\mathbf{G}\mathbf{G}'}(\mathbf{q}, \omega) = \frac{1}{V} \iint e^{i[(\mathbf{q}+\mathbf{G}')\mathbf{r}' - (\mathbf{q}+\mathbf{G})\mathbf{r}]} \varepsilon(\mathbf{r}, \mathbf{r}'; \omega) d^3r d^3r' \quad (2)$$

and the crystal volume  $V$ . The photon momenta are small compared to typical electron momenta, hence the limit  $\mathbf{q} \rightarrow \mathbf{0}$ . According to Eq. (1), we are not interested in the full inverse matrix but only in the long-wavelength limit of its reciprocal head element (i.e., the  $\mathbf{G} = \mathbf{G}' = \mathbf{0}$  component), which can be conveniently calculated by

$$\varepsilon_M(\omega) = 1 - \lim_{\mathbf{q} \rightarrow \mathbf{0}} \frac{4\pi}{q^2} \bar{L}_{\mathbf{0}\mathbf{0}}(\mathbf{q}, \omega). \quad (3)$$

We note that the right-hand side is a tensor if the material is anisotropic (bulk MoS<sub>2</sub> is an example), i.e., the macroscopic dielectric function depends on the direction  $\hat{\mathbf{q}} = \mathbf{q}/q$  along which the limit  $\mathbf{q} \rightarrow \mathbf{0}$  is taken. This direction corresponds to the light polarization vector.  $\varepsilon_M(\omega)$  is then the 3×3 dielectric tensor (and the "1" on the right-hand side the 3×3 identity matrix). If the polarization vector is defined, we know from which direction the limit  $\mathbf{q} \rightarrow \mathbf{0}$  is to be taken, and we can interpret Eq. (3) as a scalar equation.

The respective element of the modified reducible polarizability is given by

$$\bar{L}_{\mathbf{0}\mathbf{0}}(\mathbf{q}, \omega) \stackrel{\mathbf{q} \rightarrow \mathbf{0}}{\sim} \frac{q^2}{N_{\mathbf{k}}} \sum_{\lambda} |B_{\lambda}(\hat{\mathbf{q}})|^2 \times \left( \frac{1}{\omega - \Omega_{\lambda} + i\eta} - \frac{1}{\omega + \Omega_{\lambda} - i\eta} \right) \quad (4)$$

with  $N_{\mathbf{k}}$ , the number of  $\mathbf{k}$  points, and the oscillator strength

$$B_{\lambda}(\hat{\mathbf{q}}) = \sum_{\mathbf{k}} \sum_{uo} A_{\mathbf{k}uo}^{\lambda} B_{\mathbf{k}uo}(\hat{\mathbf{q}}) \quad (5)$$

and

$$B_{\mathbf{k}uo}(\hat{\mathbf{q}}) = \lim_{q \rightarrow 0} \frac{1}{q\sqrt{V_{\text{uc}}}} \langle e^{i\mathbf{q}\mathbf{r}} \varphi_{\mathbf{k}\mathbf{o}} | \varphi_{\mathbf{k}+\mathbf{q}\mathbf{u}} \rangle = \frac{1}{\sqrt{V_{\text{uc}}}} \frac{\langle \varphi_{\mathbf{k}\mathbf{o}} | -i(\hat{\mathbf{q}}\nabla) | \varphi_{\mathbf{k}\mathbf{u}} \rangle}{\epsilon_{\mathbf{k}\mathbf{u}}^0 - \epsilon_{\mathbf{k}\mathbf{o}}^0} \quad (6)$$

where  $V_{\text{uc}}$  is the unit-cell volume. Note that the factor  $q^2$  in Eq. (4) cancels out with the factor  $1/q^2$  of Eq. (3). The sum over  $o$  and  $u$  runs over occupied and unoccupied single-particle states,  $\varphi_{\mathbf{k}\mathbf{o}}(\mathbf{r}\sigma)$  and  $\varphi_{\mathbf{k}\mathbf{u}}(\mathbf{r}\sigma)$ , respectively, and  $\epsilon_{\mathbf{k}\mathbf{o}}^0$  and  $\epsilon_{\mathbf{k}\mathbf{u}}^0$  are the corresponding energy eigenvalues of the mean-field system, usually the Kohn-Sham system of DFT.

The spin index  $\sigma$  is not treated as a quantum number but included as an argument to incorporate spin-orbit coupling in the notation. The two components  $\{\varphi_{\mathbf{q}n}(\mathbf{r}\uparrow), \varphi_{\mathbf{q}n}(\mathbf{r}\downarrow)\}$  thus form spinor wavefunctions and their inner product is defined by  $\langle \dots \rangle = \sum_{\sigma} \int_V \dots d^3r$ . The wavefunctions are normalized with respect to the whole (infinite) crystal volume  $\langle \varphi_{\mathbf{k}n} | \varphi_{\mathbf{k}'n'} \rangle = \delta_{\mathbf{k}\mathbf{k}'} \delta_{nn'}$ .

The frequencies  $\Omega_{\lambda}$  and (normalized) vectors  $A_{\mathbf{k}'o'u}^{\lambda}$  are the eigensolutions of the eigenvalue problem

$$\sum_{\mathbf{k}'} \sum_{u'o'} [(\epsilon_{\mathbf{k}\mathbf{u}} - \epsilon_{\mathbf{k}\mathbf{o}}) \delta_{\mathbf{k}\mathbf{k}'} \delta_{uu'} \delta_{oo'} + \bar{v}_{\mathbf{k}\mathbf{u}, \mathbf{k}'o'; \mathbf{k}\mathbf{o}, \mathbf{k}'u'} - W_{\mathbf{k}\mathbf{u}, \mathbf{k}'o'; \mathbf{k}'u', \mathbf{k}\mathbf{o}}] A_{\mathbf{k}'u'o'}^{\lambda} = \Omega_{\lambda} A_{\mathbf{k}\mathbf{u}}^{\lambda} \quad (7)$$

with the single-particle energies  $\epsilon_{\mathbf{k}n}$ . Importantly, we have to make a distinction between the  $\epsilon_{\mathbf{k}n}$  of Eq. (7) and the mean-field eigenvalues  $\epsilon_{\mathbf{k}n}^0$ . The latter appear in Eq. (6) due to the application of  $\mathbf{k} \cdot \mathbf{p}$  perturbation theory in the last step of the derivation. They must be the exact eigenvalues of the mean-field Hamiltonian with the eigenfunctions  $\varphi_{\mathbf{k}n}(\mathbf{r})$ . The  $\epsilon_{\mathbf{k}n}$  of Eq. (7), on the other hand, are the poles of the single-particle Green function, for which one often uses a  $GW$ -renormalized Green function. In this case, the  $\epsilon_{\mathbf{k}n}$  would correspond to the  $GW$  quasiparticle energies. It is also possible to apply a scissor operator instead. The energies  $\epsilon_{\mathbf{k}n}$  would then be the "scissored" single-particle energies.

The matrix on the left-hand side of Eq. (7) can be understood as an electron-hole Hamiltonian with the interaction matrix elements

$$w_{\mathbf{k}n, \mathbf{k}'n'; \mathbf{k}-\mathbf{q}m, \mathbf{k}'+\mathbf{q}m'} = \sum_{\sigma\sigma'} \iint \varphi_{\mathbf{k}n}^*(\mathbf{r}\sigma) \varphi_{\mathbf{k}'n'}^*(\mathbf{r}'\sigma') \\ \times w(\mathbf{r}, \mathbf{r}') \varphi_{\mathbf{k}-\mathbf{q}m}(\mathbf{r}\sigma) \varphi_{\mathbf{k}'+\mathbf{q}m'}(\mathbf{r}'\sigma') d^3r d^3r', \quad (8)$$

where the generic interaction potential  $w(\mathbf{r}, \mathbf{r}')$  denotes either the modified bare Coulomb interaction  $\bar{v}(|\mathbf{r} - \mathbf{r}'|)$  or the static screened interaction  $W(\mathbf{r}, \mathbf{r}')$ . The former is defined via its Fourier transformation  $\bar{v}(\mathbf{q} + \mathbf{G}) = (1 - \delta_{\mathbf{q}+\mathbf{G}, \mathbf{0}})4\pi/|\mathbf{q} + \mathbf{G}|^2$  ( $\mathbf{G}$  are reciprocal lattice vectors), which corresponds to the bare Coulomb interaction without its long-range Fourier component. The elimination of the long-range component enables Eq. (3) [4] and is also the reason for the notation  $\bar{L}$  as a reminder of this modification. Secondly, the static screened interaction  $W(\mathbf{r}, \mathbf{r}') \equiv W(\mathbf{r}, \mathbf{r}'; \omega = 0)$  is calculated within the random-phase approximation. Its dynamic generalization  $W(\mathbf{r}, \mathbf{r}'; \omega)$  is routinely used in the  $GW$  method [16].

The BSE, written in the form of Eq. (7), can be understood as a stationary Schrödinger equation for electron-hole eigenstates. The electron-hole eigensolutions are given by the excitation energies  $\Omega_\lambda$  and their eigenvectors  $A_{\mathbf{k}o\lambda}^\lambda$ . The effective electron-hole Hamiltonian  $H$  acts on the space of two-particle wavefunctions  $\psi(\mathbf{r}\sigma, \mathbf{r}'\sigma')$ , which track the electron and hole positions. Since the set of single-particle eigenstates  $\{\varphi_{\mathbf{k}n}(\mathbf{r}\sigma)\}$  is complete, it is possible to expand  $\psi(\mathbf{r}\sigma, \mathbf{r}'\sigma')$  in terms of the products  $\{\varphi_{\mathbf{k}u}(\mathbf{r}\sigma)\varphi_{\mathbf{k}'o}^*(\mathbf{r}'\sigma')\}$ . In the present case of charge-neutral excitations with a static screened interaction, the indices  $u$  and  $o$  refer to electron (or unoccupied) and hole (or occupied) states. In the case of a non-magnetic system without spin-orbit coupling, the spin summation amounts to a spin factor 2 on the right-hand side of Eq. (4) and in front of  $\bar{v}$  in Eq. (7). We use the Tamm-Dancoff approximation, which restricts the eigenvalue spectrum to the so-called resonant electron-hole excitations  $ou \leftrightarrow o'u'$  and neglects the coupling to anti-resonant pairs  $ou \leftrightarrow u'o'$ .

### III. IMPLEMENTATION

#### A. Basis sets

We employ the LAPW basis to represent the single-particle states  $\varphi_{\mathbf{k}n}(\mathbf{r}\sigma)$ . The FLAPW method[24–26] divides space into two regions, the non-overlapping atom-centered muffin-tin (MT) spheres and the remaining interstitial region. In the latter, the basis functions are simple plane waves  $e^{i(\mathbf{k}+\mathbf{G})\mathbf{r}}/\sqrt{V}$  with a reciprocal cutoff radius  $|\mathbf{k} + \mathbf{G}| \leq G_{\max}$ . These plane waves are matched in value and gradient to linear combinations of numerical functions  $u_{lp}(r)Y_{lm}(\hat{\mathbf{r}})$  in the MT spheres ( $\mathbf{r}$  measured from the MT center). Here,  $Y_{lm}(\hat{\mathbf{r}})$  are spherical harmonics, and  $u_{lp}^\sigma(r)$  are numerical functions defined on a radial grid. The  $l$  quantum numbers are bounded from above  $0 \leq l \leq l_{\max}$ , where  $l_{\max}$  is a convergence parameter. The index  $p$  enumerates different radial functions. The standard LAPW basis employs  $u_{l0}^\sigma(r)$ , which is the solution of the radial scalar-relativistic Dirac equation with the spherically averaged spin- $\sigma$  effective Kohn-Sham potential inside the MT sphere, and its energy derivative  $u_{l1}^\sigma(r)$ . So-called local orbitals [27]  $u_{lp}^\sigma(r)$  with  $p \geq 2$  can be included to augment the basis in the MT spheres [27]. No approximations are made to the shape of the effective potential [26].

As already discussed in the previous section, we formulate the BSE as an eigenvalue problem [Eq. (7)] in a two-particle product basis, defined as pairs of occupied and unoccupied states

$$\psi_{\mathbf{k}uo}(\mathbf{r}\sigma, \mathbf{r}'\sigma') = \varphi_{\mathbf{k}u}(\mathbf{r}\sigma)\varphi_{\mathbf{k}'o}^*(\mathbf{r}'\sigma'). \quad (9)$$

Formally, the single-particle wavefunctions are orthonormal and complete in the electron Hilbert space. This implies that the two-particle product basis is orthonormal and complete in the electron-hole Hilbert space with the orthonormality condition

$$\langle \psi_{\mathbf{k}uo} | \psi_{\mathbf{k}'u'o'} \rangle = \langle \varphi_{\mathbf{k}u} | \varphi_{\mathbf{k}'u'} \rangle \langle \varphi_{\mathbf{k}o} | \varphi_{\mathbf{k}'o'} \rangle = \delta_{\mathbf{k}\mathbf{k}'} \delta_{uu'} \delta_{oo'}. \quad (10)$$

As a third basis set, we introduce the mixed basis [15, 16], which is designed to represent wavefunction products of the form  $\varphi_{\mathbf{k}u}(\mathbf{r}\sigma)\varphi_{\mathbf{k}'o}^*(\mathbf{r}\sigma')$ . In contrast to the electron-hole basis function of Eq. (9), the two single-particle wavefunctions are evaluated at the same point in space  $\mathbf{r}$  and the same spin  $\sigma$  (but not necessarily at the same  $\mathbf{k}$ ). The mixed basis is helpful for the evaluation of the interaction matrix elements Eq. (8), in which there are two pairs of wavefunctions that have the same space and spin arguments. While the two-particle product basis of Eq. (9) is orthonormal, the same- $\mathbf{r}$ -same- $\sigma$  products are highly linearly dependent, which is why they cannot directly be used as a basis set. Instead, the mixed basis is constructed directly from products of LAPW basis functions: plane waves  $e^{i(\mathbf{k}+\mathbf{G})\mathbf{r}}/\sqrt{V}$  in the interstitial (with a cutoff  $|\mathbf{k} + \mathbf{G}| \leq G'_{\max}$ ) matched to linear combinations of  $M_{LP}(r)Y_{LM}(\hat{\mathbf{r}})$  with  $0 \leq L \leq L_{\max}$ . The radial functions  $M_{LP}(r)$  are constructed from products

$u_p^\sigma(r)u_{p'}^\sigma(r)$  with  $|l-l'| \leq L \leq l+l'$ . Linear dependencies are eliminated in each  $L$  channel to optimize the MT basis. (We note that the mixed-basis functions are defined in a spin-independent manner. In case of spin polarization, both products  $u^\uparrow u^\uparrow$  and  $u^\downarrow u^\downarrow$  are included in the construction so that not only the products themselves but also differences such as  $u^\uparrow u^\uparrow - u^\downarrow u^\downarrow$  or mixed products  $u^\uparrow u^\downarrow$  can be well represented in the basis.) The mixed-basis functions, denoted by  $M_I^{\mathbf{q}}(\mathbf{r})$  with an index  $I$ , are not orthonormal in the interstitial region so that a second dual basis set  $\{\tilde{M}_I^{\mathbf{q}}(\mathbf{r})\}$  needs to be considered. Together they fulfill the completeness relations

$$\sum_{\mathbf{q}} \sum_I |M_I^{\mathbf{q}}\rangle \langle \tilde{M}_I^{\mathbf{q}}| = 1, \quad \langle M_I^{\mathbf{q}} | \tilde{M}_J^{\mathbf{q}'} \rangle = \delta_{\mathbf{q}\mathbf{q}'} \delta_{IJ} \quad (11)$$

For more details about the mixed basis, the reader is referred to Refs. 15–17.

## B. Coulomb divergence

With the completeness relation Eq. (11), the interaction matrix elements Eq. (8) can be evaluated as vector-matrix-vector products

$$w_{\mathbf{k}n, \mathbf{k}'n'; \mathbf{k}-\mathbf{q}m, \mathbf{k}'+\mathbf{q}m'} = \frac{1}{N_{\mathbf{k}}} \sum_{IJ} \langle \varphi_{\mathbf{k}n} | \varphi_{\mathbf{k}-\mathbf{q}m} M_{\mathbf{q}I} \rangle \times \langle \tilde{M}_{\mathbf{q}I} | w | \tilde{M}_{\mathbf{q}J} \rangle \langle M_{\mathbf{q}J} \varphi_{\mathbf{k}'n'} | \varphi_{\mathbf{k}'+\mathbf{q}m'} \rangle. \quad (12)$$

The matrix  $\langle \tilde{M}_{\mathbf{q}I} | w | \tilde{M}_{\mathbf{q}J} \rangle$  is precalculated. The prefactor  $N_{\mathbf{k}}^{-1}$  originates from the mixed-basis representation  $w(\mathbf{r}, \mathbf{r}') = (N_{\mathbf{k}})^{-1} \sum_{\mathbf{k}, I, J} \langle \tilde{M}_{\mathbf{k}I} | w | \tilde{M}_{\mathbf{k}J} \rangle M_{\mathbf{k}I}(\mathbf{r}) M_{\mathbf{k}J}^*(\mathbf{r}')$ . The computation of the vectors  $\langle M_{\mathbf{q}I} \varphi_{\mathbf{k}n} | \varphi_{\mathbf{k}+\mathbf{q}m} \rangle$  and the vector-matrix-vector products in Eq. (12) are among the most expensive steps of the whole calculation. In Sec. III C 2, we will use symmetry operations to accelerate these computations.

By calculating the interaction matrix elements using the mixed basis, SPEX maintains the all-electron description and avoids a mapping to a pure plane-wave basis. One may wonder why previous FLAPW implementations chose a plane-wave basis. An aspect in this choice might have been the fact that the Coulomb interaction is long-range, which gives rise to singularities in the Coulomb matrix. The plane-wave representation has the advantage that there is only one divergent element, namely the head element ( $\mathbf{G} = \mathbf{G}' = \mathbf{0}$ ), in the bare Coulomb matrix, and the screened interaction additionally has divergent wing elements ( $\mathbf{G} = \mathbf{0}$  or  $\mathbf{G}' = \mathbf{0}$ ) of lower order. This simple structure is lost in the mixed-basis representation. However, it can be recovered if a unitary transformation from the mixed basis to the Coulomb eigenbasis is performed [28]. The mixed basis is defined in such a way that this transformation leads to the same matrix structure as in the pure plane-wave basis with divergent head and wing elements, while all other matrix elements

remain finite. We can thus treat the Coulomb singularity as if we had a pure plane-wave basis.

According to the Eqs. (7) and (8), one needs matrix elements of  $w = \bar{v}$  only for  $\mathbf{q} = \mathbf{0}$ , whereas the matrix elements of  $w = W$  are required for all elements of the  $\mathbf{q}$ -point set because of the condition  $\mathbf{q} = \mathbf{k} - \mathbf{k}'$ , and  $\mathbf{k}'$  runs over all wave vectors. Since  $\bar{v}$  is a modified Coulomb potential that specifically lacks the long-range Fourier component, there is no singularity in  $\bar{v}$ . However, the divergent elements of  $W$  do play a role.

In the limit of small momentum transfers  $\mathbf{q}$ , the projections  $\langle e^{i\mathbf{q}\mathbf{r}} \varphi_{\mathbf{k}n} | \varphi_{\mathbf{k}+\mathbf{q}n'} \rangle$  of the hole-hole ( $n = o, n' = o'$ ) and electron-electron products ( $n = u, n' = u'$ ) onto the plane wave  $e^{i\mathbf{q}\mathbf{r}}$  are approximately 1 if the band indices are equal ( $o = o'$  or  $u = u'$ ) (orthonormality) and proportional to  $q$  if the band indices differ ( $o \neq o'$  or  $u \neq u'$ ) ( $\mathbf{k} \cdot \mathbf{p}$  perturbation theory). To be more precise, the proportionality in the latter case has the form  $\mathbf{a}\mathbf{q}$  with a vector  $\mathbf{a}$ . As a consequence, divergent terms proportional to  $1/q^2$  formally appear in the diagonal elements of the BSE electron-hole Hamiltonian [Eq. (7)] where  $u = u'$ ,  $o = o'$ , and  $\mathbf{k} = \mathbf{k}'$ . All other divergent contributions vanish: The wing elements behave as  $\mathbf{b}\hat{\mathbf{q}}/q$  (with some other vector  $\mathbf{b}$ ), which, combined with the diagonal case  $o = o'$  and  $u = u'$ , integrates to zero. Likewise, the combination of  $1/q^2$  and  $o = o'$ ,  $u \neq u'$  or  $o \neq o'$ ,  $u = u'$  gives rise to the same kind of divergence  $\mathbf{a}\hat{\mathbf{q}}/q$  and thus also integrates to zero.

We are thus left with the  $1/q^2$  terms in the diagonal matrix elements. Of course, actual singular elements should not appear in the BSE Hamiltonian. To get an understanding of how to treat the singularity appropriately, we push the size of the simulation cell, in which periodic boundary conditions shall hold for any finite size, to infinity. As a consequence, the wave vector  $\mathbf{k}$ , which can assume only discrete (vector) values in finite simulation cells, becomes a continuous variable. The infinite simulation cell, together with a continuous wave vector  $\mathbf{k}$ , eventually allows the exciton to be truly localized, and it also resolves the problem of the long-range divergence, because integrating over it in reciprocal space leads to a finite value. Viewed from a different perspective, when considering a finite  $\mathbf{k}$ -point set, we can imagine the integrand to be interpolated between the discrete  $\mathbf{k}$  points. This interpolation effectively averages over the divergent part of  $W$  and identifies each basis function  $\psi_{\mathbf{k}u o}$  with a localized wave packet consisting of continuous momenta centered around each discrete  $\mathbf{k}$  point. The  $\mathbf{k}'$  summation of Eq. (7), when regarded as an integration over a wave vector, not only includes the point  $\mathbf{k}' = \mathbf{k}$  ( $\mathbf{q} = \mathbf{0}$ ) but also all points in its neighborhood. In a manner of speaking, the form of the divergence is mapped out in the  $\mathbf{k}'$  integration.

The divergence is limited to the  $\mathbf{G} = \mathbf{G}' = \mathbf{0}$  component of  $W$  and has the form

$$W_{\mathbf{0}\mathbf{0}}(\mathbf{q}) = \frac{4\pi}{q^2} \frac{1}{\hat{\mathbf{q}}^T \mathbf{L} \hat{\mathbf{q}}} \quad (13)$$

around  $\mathbf{q} = \mathbf{0}$  with  $\hat{\mathbf{q}} = \mathbf{q}/q$  and a  $3 \times 3$  tensor  $\mathbf{L}$  [16, 29]. (We note again that  $W$  is  $\omega$  dependent in general, and so is  $\mathbf{L}$ , but this  $\omega$  dependence is omitted due to the static approximation employed in the BSE.) Clearly, integrating over a  $q^{-2}$  divergence in 3D yields a finite value, but the question arises over which region to integrate. To avoid double counting, the integration region should be somehow limited to  $\mathbf{q} = \mathbf{0}$  and its neighborhood without including any of the non-zero  $\mathbf{q}$  points of the  $\mathbf{q}$  mesh, since each  $\mathbf{q}$  point possesses its own matrix element in Eq. (7). One might consider integrating over a region stretching halfway to the neighboring  $\mathbf{q}$  points. To simplify the integration, one might furthermore define the integration region to be spherical. However, we find that such a treatment of the divergence gives rise to bad  $\mathbf{q}$ -point convergence. Furthermore, it would not account for anisotropic (e.g., layered) systems or unevenly distributed  $\mathbf{q}$ -point meshes.

We basically employ the same treatment of the divergence as the one introduced in Ref. 16 for the  $GW$  method. Here, we describe an extended version that allows for anisotropy in the screening, i.e., tensors  $\mathbf{L}$  that are not just a multiple of the identity matrix. The basic idea is that the region of integration is extended over the whole reciprocal space. As this integration comprises all other  $\mathbf{q}$  points, too, we have to introduce a double-counting correction. Another difficulty is that  $q^{-2}$  does not integrate to a finite value if the integration extends over the whole space. We address this difficulty by replacing  $1/q^2$  in Eq. (13) by  $e^{-bq^2}/q^2$  with a small parameter  $b > 0$ . This is a modification of an idea introduced in Ref. 30 in the context of the Hartree-Fock method. The exponential factor guarantees that both integral and  $\mathbf{q}$  sum remain finite in the contribution of the singularity

$$W_{\mathbf{kn}, \mathbf{kn}'; \mathbf{kn}, \mathbf{kn}'}^{\text{div}} = \frac{1}{2\pi^2} \int d^3q \frac{e^{-bq^2}}{q^2 \hat{\mathbf{q}}^T \mathbf{L} \hat{\mathbf{q}}} - \frac{4\pi}{N_{\mathbf{k}} V_{\text{uc}}} \sum_{q \neq 0} \frac{e^{-bq^2}}{q^2 \hat{\mathbf{q}}^T \mathbf{L} \hat{\mathbf{q}}} \quad (14)$$

to the diagonal terms of Eq. (12) for  $w = W$ , where the sum over  $\mathbf{q}$  is the double-counting correction. To evaluate the integral, we first consider the angular integration. The only angle-dependent term is  $\hat{\mathbf{q}}^T \mathbf{L} \hat{\mathbf{q}}$ . Its expansion in terms of spherical harmonics can be written as

$$\hat{\mathbf{q}}^T \mathbf{L} \hat{\mathbf{q}} = \sum_{l=0,2} \sum_{m=-l}^l L_{lm} Y_{lm}(\hat{\mathbf{q}}). \quad (15)$$

Likewise, we make the general ansatz

$$\frac{1}{\hat{\mathbf{q}}^T \mathbf{L} \hat{\mathbf{q}}} = \sum_{l=0,2,4,\dots} \sum_{m=-l}^l H_{lm} Y_{lm}(\hat{\mathbf{q}}) \quad (16)$$

for its reciprocal with unknown coefficients  $H_{lm}$ . Multiplication and using the Gaunt coefficients  $G_{LM,lm,l'm'}$  =

$\int Y_{LM}^*(\hat{\mathbf{q}}) Y_{lm}(\hat{\mathbf{q}}) Y_{l'm'}(\hat{\mathbf{q}}) d^2 \hat{\mathbf{q}}$  gives

$$1 = \sum_{L=0,2,4,\dots} \sum_{M=-L}^L \left[ \sum_{l=0,2} \sum_{m=-l}^l \sum_{l'=|L-l|}^{L+l} G_{LM,lm,l',M-m} \times L_{lm} H_{l',M-m} \right] Y_{LM}(\hat{\mathbf{q}}), \quad (17)$$

which, by equating the coefficients on both sides [note that  $\sqrt{4\pi} Y_{00}(\hat{\mathbf{q}}) = 1$ ], yields a system of linear equations. The upper bound of the  $l$  sum ( $L$  sum) in Eq. (16) [Eq. (17)] is a convergence parameter. Since all  $Y_{lm}(\hat{\mathbf{q}})$  integrate to zero on the unit sphere except  $Y_{00}(\hat{\mathbf{q}})$ , it is sufficient to converge only the coefficient  $H_{00}$  with respect to the summation upper bound. We find that convergence is very fast. Using the spherical-harmonic expansions of Eqs. (15) and (16) generally accounts for anisotropic dielectric screening.

We finally get

$$\int_{q < q_{\text{max}}} d^3q \frac{e^{-bq^2}}{q^2 \hat{\mathbf{q}}^T \mathbf{L} \hat{\mathbf{q}}} = \pi \frac{H_{00}}{\sqrt{b}} \text{erf}(\sqrt{b} q_{\text{max}}). \quad (18)$$

with the error function  $\text{erf}(x) = (2/\sqrt{\pi}) \int_0^x e^{-x'^2} dx'$ . We have introduced a cutoff radius  $q_{\text{max}}$  up to which the  $\mathbf{q}$  integration and summation are carried out. The reason for introducing  $q_{\text{max}}$  is that, even with the exponential factor, the addends do not fall off quickly enough to enable a fast evaluation of the  $\mathbf{q}$  sum. In addition, we smoothen the upper limit of the sum by an additional function

$$\sum_{\substack{q \neq 0 \\ q < q_{\text{max}} - \Delta}} \frac{e^{-bq^2}}{q^2 \hat{\mathbf{q}}^T \mathbf{L} \hat{\mathbf{q}}} + \sum_{\substack{q \neq 0 \\ |q - q_{\text{max}}| \leq \Delta}} \frac{e^{-bq^2}}{q^2 \hat{\mathbf{q}}^T \mathbf{L} \hat{\mathbf{q}}} f\left(\frac{q - q_{\text{max}}}{\Delta}\right) \quad (19)$$

with  $\Delta = (V_{\text{BZ}}/N_{\mathbf{k}})^{1/3}$ , the Brillouin-zone volume  $V_{\text{BZ}} = 8\pi^3/V_{\text{uc}}$ , and  $f(x) = (x^3 - 3x + 2)/4$ . To minimize the number of parameters,  $b$  and  $q_{\text{max}}$  are linked by the condition  $b = e^{-bq_{\text{max}}^2}$ . We have found  $b = 0.005$  to be a good choice.

### C. Usage of symmetries

BSE calculations are computationally demanding. The most expensive steps are (1) the calculation of the screened interaction within the random-phase approximation, (2) the construction of the electron-hole Hamiltonian Eqs. (7) and (8), and finally (3) the diagonalization of the electron-hole Hamiltonian. All of these steps can be significantly accelerated by exploiting spatial and time-reversal symmetries, which is an elegant way of reducing the computational burden without sacrificing accuracy.

How spatial and time-reversal symmetries can be utilized in the calculation of the screened interaction has

already been described in Ref. 16. For the sake of completeness, we note that we make use of the block-diagonal structure of  $W$  in the basis of Coulomb eigenfunctions  $\{C_{\mathbf{k}\mu}\}$ :  $\langle C_{\mathbf{k}\mu}|W|C_{\mathbf{k}\nu}\rangle = 0$  unless  $C_{\mathbf{k}\mu}(\mathbf{r})$  and  $C_{\mathbf{k}\nu}(\mathbf{r})$  fall into the same irreducible representation (irrep) of group theory. The Coulomb eigenfunctions are defined as linear combinations of the mixed-basis functions  $C_{\mathbf{q}\mu}(\mathbf{r}) = \sum_I c_{\mathbf{q},\mu I} M_{\mathbf{q}I}(\mathbf{r})$  with the matrix  $c_{\mathbf{q},\mu I}$  of eigenvectors of  $v_{\mathbf{q},IJ} = \langle M_{\mathbf{q}I}|v|M_{\mathbf{q}J}\rangle$ . Obviously,  $\bar{v}$  becomes diagonal in this basis. We will discuss irreps in Sec. III C 3 in more detail. Presently, it suffices to understand the irreps as a classification scheme that allows us to bring the matrix representation of  $W$  into block-diagonal form. A similar technique can be used for nonlocal operators [18] in general, including the  $GW$  self-energy. The block-diagonal structure of  $W$  accelerates the evaluation of matrix-matrix products. However, since this aspect is not the focus of the present paper, we defer a more detailed discussion to future work.

The evaluation of the matrix elements Eq. (12) is the most expensive step in the construction of the electron-hole Hamiltonian of Eq. (7). Fortunately, many of the  $W$  matrix elements are related to each other via symmetry operations. Thus, instead of calculating all matrix elements explicitly, we may calculate only a few and generate the other elements from these with the help of symmetry transformations.

Furthermore, we apply group theoretical tools to make the two-particle Hamiltonian block-diagonal and, in this way, speed up the diagonalization of the Hamiltonian. It is important to note that, in this case, the Hamiltonian is a two-particle Hamiltonian. It is represented in a basis of two-particle functions, each depending on two points in space (see Sec. III A). So, the block-diagonality of the electron-hole Hamiltonian goes beyond what was explained above about the  $W$  matrix, which is represented in mixed-basis functions, i.e., regular local functions that depend on a single point in space. To bring the Hamiltonian into block-diagonal form, we have to perform a unitary transformation of the product functions. The new functions — linear combinations of Eq. (9) — can then be classified uniquely into irreps.

### 1. Symmetry transformation matrix

Before explaining the techniques in detail, we introduce the notation. We write a crystal symmetry operation as  $s = (A, \mathbf{T} + \mathbf{a}, \alpha)$  with a  $3 \times 3$  (proper or improper) rotation matrix  $A \in O(3)$ , a lattice vector  $\mathbf{T}$ , a translation vector  $\mathbf{a}$  (which is not a lattice vector), and  $\alpha$ , which is 0 (1) if the symmetry operation excludes (includes) time reversal. The complete set of symmetry operations forms a symmetry group  $S$ .

The action of a symmetry operation on a real-space and reciprocal-space vector as well as on a single-particle

function  $\varphi(\mathbf{r}\sigma)$  is declared as

$$s\mathbf{r} = A\mathbf{r} + \mathbf{T} + \mathbf{a} \quad (20)$$

$$s\mathbf{k} = (-1)^\alpha A\mathbf{k} + \bar{\mathbf{G}} \quad (21)$$

$$s\varphi(\mathbf{r}\sigma) = \sum_{\sigma'} B_{\sigma\sigma'} c^\alpha \varphi(s^{-1}\mathbf{r}, \sigma') \quad (22)$$

with  $s^{-1}\mathbf{r} = A^{-1}(\mathbf{r} - \mathbf{T} - \mathbf{a})$  and the conjugation operator  $c$  [ $c^0 f(\mathbf{r}) = f(\mathbf{r})$  and  $c^1 f(\mathbf{r}) = f^*(\mathbf{r})$ ]. The vector  $\bar{\mathbf{G}}$  (if not the nullvector) folds the  $\mathbf{k}$  vector back into the first Brillouin zone. Obviously,  $\bar{\mathbf{G}}$  depends on  $s$  and  $\mathbf{k}$  but has been written without these dependencies to simplify the notation. The matrix  $B \in \text{SU}(2)$  is the  $2 \times 2$  rotation matrix in spin space, which derives from  $A$  and  $\alpha$ . If spin-orbit coupling is neglected, the  $B$  matrix is simply the identity matrix.

When we let a symmetry operation  $s$  that leaves the Hamiltonian invariant act on an eigenstate, it maps this eigenstate onto another eigenstate with the same energy eigenvalue. The symmetry transformation, when represented in the basis of eigenstates, is thus a sparse unitary matrix, which only mixes degenerate states

$$s\varphi_{\mathbf{k}n}(\mathbf{r}\sigma) = \sum_{n' \sim n} \Gamma(s)_{\mathbf{k}n}^{\mathbf{k}'n'} \varphi_{\mathbf{k}'n'}(\mathbf{r}\sigma), \quad (23)$$

where  $\mathbf{k}' = s\mathbf{k}$  and the notation  $n' \sim n$  means that  $n'$  runs over all states at  $s\mathbf{k}$  [Eq. (21)] that are (energy) degenerate with the  $n$ th state at  $\mathbf{k}$ . It suffices to calculate  $\Gamma(s)_{\mathbf{k}n}^{\mathbf{k}'n'} = \langle \varphi_{\mathbf{k}'n'} | s\varphi_{\mathbf{k}n} \rangle$  for the generators  $\{s_\nu\}$  of  $S$ . The generators are elements of  $S$  from which all symmetry operations can be generated: For any  $s \in S$ , there is a representation  $s = s_\nu s_{\nu'} s_{\nu''} \dots$  (some of the generators may be identical). The transformation  $\Gamma(s)$  can then be constructed by multiplication  $\Gamma(s) = \Gamma(s_\nu)\Gamma(s_{\nu'})\Gamma(s_{\nu''}) \dots$  (in simplified notation). The number of generators of  $S$  is usually much smaller than the total number of operations in  $S$ .

Applying the symmetry transformation to an electron-hole basis function yields

$$s[\varphi_{\mathbf{k}u}(\mathbf{r}\sigma)\varphi_{\mathbf{k}o}^*(\mathbf{r}'\sigma')] = \sum_{u' \sim u} \sum_{o' \sim o} \tilde{\Gamma}(s)_{\mathbf{k}uo}^{\mathbf{k}'u'o'} \varphi_{\mathbf{k}'u'}(\mathbf{r}\sigma)\varphi_{\mathbf{k}'o'}^*(\mathbf{r}'\sigma') \quad (24)$$

again with a sparse unitary transformation matrix

$$\tilde{\Gamma}(s)_{\mathbf{k}uo}^{\mathbf{k}'u'o'} = \Gamma(s)_{\mathbf{k}u}^{\mathbf{k}'u'} \Gamma^*(s)_{\mathbf{k}o}^{\mathbf{k}'o'}. \quad (25)$$

The full symmetry group  $S$  has thus representations  $\tilde{\Gamma}(s)$  of unitary and anti-unitary operators in the space of electron-hole wavefunction products. The translations  $s_{\mathbf{T}} : \mathbf{r} \mapsto \mathbf{r} + \mathbf{T} \in S_{\mathbf{T}}$  have a trivial representation

$$\tilde{\Gamma}(s_{\mathbf{T}})_{\mathbf{k}uo}^{\mathbf{k}'u'o'} = \delta_{uu'} e^{i\mathbf{T}\mathbf{k}} \delta_{oo'} e^{-i\mathbf{T}\mathbf{k}} = \delta_{uu'} \delta_{oo'}. \quad (26)$$

We can therefore switch from  $S$  to the group quotient  $S/S_{\mathbf{T}}$ , which removes the lattice translations. The resulting quotient group is now finite and the representations  $\tilde{\Gamma}(sS_{\mathbf{T}})$  of the coset  $sS_{\mathbf{T}}$  are simply  $\tilde{\Gamma}(s)$ . For simplicity, we will refer to the quotient group as  $S$  in the following.

## 2. Hamiltonian matrix elements

The effective electron-hole Hamiltonian matrix and its elements must obey the crystal symmetries. This fact can be used to accelerate its construction. We first turn to the screened interaction matrix  $W$ . Let us consider a matrix element  $W_{\mathbf{k}'u, \mathbf{k}o'; \mathbf{k}u', \mathbf{k}'o}$  (note the change of notation  $\mathbf{k} \leftrightarrow \mathbf{k}'$  with respect to Eq. 7). Comparison with Eq. (8) gives  $\mathbf{k}' = \mathbf{k} + \mathbf{q}$  and shows that the  $w$  matrix (here,  $w = W$ ) depends on  $\mathbf{q}$ . The loop over  $\mathbf{q}$  should be the outer loop. We restrict  $\mathbf{q}$  to the irreducible Brillouin zone (IBZ), which is the minimal set of  $\mathbf{k}$  points from which all other  $\mathbf{k}$  points can be generated via Eq. (21). In addition, we restrict  $\mathbf{k}$  to the *extended irreducible Brillouin zone* [EIBZ( $\mathbf{q}$ )], which is the minimal set of  $\mathbf{k}$  points from which all other  $\mathbf{k}$  points can be generated via Eq. (21) with the restriction that the operations  $s$  are elements of the so-called "little group". The little group is a subgroup of  $S$ , which contains all symmetry operations  $s$  that map  $\mathbf{q}$  onto itself,  $s\mathbf{q} = \mathbf{q}$ . In general, the EIBZ( $\mathbf{q}$ ) is larger than the IBZ because the little group is smaller than the full symmetry group.

We now show that all other matrix elements (with  $\mathbf{q} \in \text{BZ}$  and  $\mathbf{k} \in \text{BZ}$ ) can be generated from the subset [ $\mathbf{q} \in \text{IBZ}$  and  $\mathbf{k} \in \text{EIBZ}(\mathbf{q})$ ] by applying suitable symmetry operations. Given general  $\mathbf{q}$  and  $\mathbf{k}$ , there is a symmetry operation  $s'$  that rotates  $\mathbf{q}$  into the IBZ,  $\mathbf{q}' = s'\mathbf{q}$ , and there is another symmetry operation  $s''$  of the little group that rotates  $s'\mathbf{k}$  into the EIBZ( $\mathbf{q}'$ ). By definition of the little group,  $s''$  leaves  $\mathbf{q}'$  invariant, and we have  $\mathbf{q}' = s\mathbf{q} \in \text{IBZ}$  and  $\mathbf{k}' = s\mathbf{k} \in \text{EIBZ}(\mathbf{q}')$  with  $s = s''s'$ .

Let us write an arbitrary matrix element as  $\langle \varphi_{\mathbf{k}+\mathbf{q}u} \varphi_{\mathbf{k}o'} | W | \varphi_{\mathbf{k}u'} \varphi_{\mathbf{k}+qo} \rangle$ . Substitution of the integration variables  $\mathbf{r} \rightarrow s^{-1}\mathbf{r}$  (likewise for  $\mathbf{r}'$ ) does not change the integral. Then, using Eq. (22), the symmetry invariance of  $W(\mathbf{r}, \mathbf{r}')$  ( $s W s^\dagger = W$ ), and the fact that  $W(\mathbf{r}, \mathbf{r}')$  is real, we can write

$$\begin{aligned} & \langle \varphi_{\mathbf{k}+\mathbf{q}u} \varphi_{\mathbf{k}o'} | W | \varphi_{\mathbf{k}u'} \varphi_{\mathbf{k}+qo} \rangle & (27) \\ &= c^\alpha \langle s\varphi_{\mathbf{k}+\mathbf{q}u} s\varphi_{\mathbf{k}o'} | W | s\varphi_{\mathbf{k}u'} s\varphi_{\mathbf{k}+qo} \rangle \\ &= c^\alpha \sum_{\substack{u'' \sim u \\ u' \sim u'}} \sum_{\substack{o'' \sim o \\ o' \sim o}} \Gamma^*(s)_{\mathbf{k}+\mathbf{q}u}^{\mathbf{k}'+\mathbf{q}'u''} \Gamma^*(s)_{\mathbf{k}o'}^{\mathbf{k}'o''} \Gamma(s)_{\mathbf{k}u'}^{\mathbf{k}'u''} \\ & \Gamma(s)_{\mathbf{k}+qo}^{\mathbf{k}'+\mathbf{q}'o''} \langle \varphi_{\mathbf{k}'+\mathbf{q}'u''} \varphi_{\mathbf{k}'o''} | W | \varphi_{\mathbf{k}'u''} \varphi_{\mathbf{k}'+\mathbf{q}'o''} \rangle \end{aligned}$$

with the irreducible representations Eq. (23). We have taken into account the possibility of  $\alpha = 1$ , i.e., the symmetry operation  $s$  involves time reversal. The spin rotation matrix  $B_{\sigma\sigma'}$  can be ignored because the integrals of the form  $\langle \varphi | \varphi M \rangle$  in Eq. (8) involve a trace over the spins (in the SOC case), which is invariant with respect to SU(2) spin rotations. Since the four summations only run over the degenerate subspaces (including a maximum of three states), Eq. (27) requires practically no computing time.

In practice, we loop over  $\mathbf{q}' \in \text{IBZ}$  and  $\mathbf{k}' \in \text{EIBZ}(\mathbf{q}')$  and calculate the corresponding matrix elements of the

right-hand-side of Eq. (7), which we call the "seed" matrix elements. For each pair  $(\mathbf{k}', \mathbf{k}' + \mathbf{q}')$ , we determine a minimal set of symmetry operations  $\{s_1, s_2, \dots\}$  with which all pairs  $(\mathbf{k}_1, \mathbf{k}_2)$  symmetry equivalent to  $(\mathbf{k}', \mathbf{k}' + \mathbf{q}')$  can be generated, e.g.,  $\mathbf{k}_1 = s_1\mathbf{k}'$  and  $\mathbf{k}_2 = s_1(\mathbf{k}' + \mathbf{q}')$ . Here, "minimal" means that if there is another  $s$  that would generate the same pair, this  $s$  is discarded from the set. The set does *not* form a subgroup, since, for example, the neutral element is not an element of the set. We then loop over  $s_1, s_2$ , etc. and calculate the corresponding "rotated" matrix elements following Eq. (27). In this way, all matrix elements of the screened Coulomb interaction are calculated.

An analogous strategy is applied to the matrix elements of the (modified) bare Coulomb interaction  $\bar{v}_{\mathbf{k}u, \mathbf{k}'o'; \mathbf{k}o, \mathbf{k}'u'}$ . Furthermore, it is possible to accelerate the computation of the seed matrix elements. The different order of  $\mathbf{k}$  indices compared to  $W_{\mathbf{k}'u, \mathbf{k}o'; \mathbf{k}u', \mathbf{k}'o}$  leads us to another strategy to evaluate them, namely one that minimizes the number of integrals  $\langle M\varphi | \varphi \rangle$  and matrix-vector products. A comparison to Eq. (12) (now,  $w = \bar{v}$ ) shows that  $\mathbf{q} = \mathbf{0}$ . If symmetry is used to distribute the matrix elements as in the case of  $W_{\mathbf{k}'u, \mathbf{k}o'; \mathbf{k}u', \mathbf{k}'o}$ , then  $\mathbf{k} \in \text{IBZ}$  and  $\mathbf{k}' \in \text{EIBZ}(\mathbf{k})$ . However, it is simpler in a first implementation to generate all matrix elements explicitly. Therefore, we adopt the more general assumption  $\mathbf{k} \in \text{BZ}$  and  $\mathbf{k}' \in \text{BZ}$  in the following. First, we calculate the integrals  $\langle M_{\mathbf{0}I} \varphi_{\mathbf{k}n} | \varphi_{\mathbf{k}m} \rangle$  for all  $\mathbf{k} \in \text{IBZ}$  and multiply them with the Coulomb matrix

$$[\tilde{M}_{\mathbf{0}I} \varphi_{\mathbf{k}n} | \varphi_{\mathbf{k}m}] := \sum_J \langle \tilde{M}_{\mathbf{0}I} | \bar{v} | \tilde{M}_{\mathbf{0}J} \rangle \langle M_{\mathbf{0}J} \varphi_{\mathbf{k}n} | \varphi_{\mathbf{k}m} \rangle. \quad (28)$$

Here, we can make use of a sparse representation of the  $\bar{v}$  matrix [18]. Obviously, the matrix elements for  $\mathbf{k} \in \text{IBZ}$  and  $\mathbf{k}' \in \text{IBZ}$  can be obtained directly by scalar products

$$\bar{v}_{\mathbf{k}u, \mathbf{k}'o'; \mathbf{k}o, \mathbf{k}'u'} = \sum_I \langle \varphi_{\mathbf{k}u} | \varphi_{\mathbf{k}o} M_{\mathbf{0}I} \rangle [\tilde{M}_{\mathbf{0}I} \varphi_{\mathbf{k}'o'} | \varphi_{\mathbf{k}'u'}] \quad (29)$$

For  $\mathbf{k}$  outside the IBZ, the wavefunctions  $\varphi_{\mathbf{k}n}(\mathbf{r}\sigma)$  are not stored in computer memory, but they are generated by the operation  $\varphi_{\mathbf{k}n}(\mathbf{r}\sigma) = s_{\mathbf{k}} \varphi_{\mathbf{p}_{\mathbf{k}n}}(\mathbf{r}\sigma)$  according to Eq. (22) with a suitable operation  $s_{\mathbf{k}}$  and  $\mathbf{p}_{\mathbf{k}} \in \text{IBZ}$  ( $\mathbf{p}_{\mathbf{k}}$  is the "parent" of  $\mathbf{k}$  with  $s_{\mathbf{k}}\mathbf{p}_{\mathbf{k}} = \mathbf{k}$ ). With an analogous notation as the one used above for the  $W$  matrix elements, we thus have

$$\begin{aligned} & \langle \varphi_{\mathbf{k}u} \varphi_{\mathbf{k}o} | \bar{v} | \varphi_{\mathbf{k}'o'} \varphi_{\mathbf{k}'u'} \rangle & (30) \\ &= \langle s_{\mathbf{k}} \varphi_{\mathbf{p}_{\mathbf{k}}u} s_{\mathbf{k}} \varphi_{\mathbf{p}_{\mathbf{k}}o} | \bar{v} | s_{\mathbf{k}'} \varphi_{\mathbf{p}_{\mathbf{k}'o'}} s_{\mathbf{k}'} \varphi_{\mathbf{p}_{\mathbf{k}'u'}} \rangle \\ &= c^\alpha \langle \varphi_{\mathbf{p}_{\mathbf{k}}u} \varphi_{\mathbf{p}_{\mathbf{k}}o} | \bar{v} | s \varphi_{\mathbf{p}_{\mathbf{k}'o'}} s \varphi_{\mathbf{p}_{\mathbf{k}'u'}} \rangle, \end{aligned}$$

where  $s = s_{\mathbf{k}}^{-1} s_{\mathbf{k}'}$ , and  $\alpha = 1$  takes into account time reversal in the symmetry operation  $s_{\mathbf{k}}$ , otherwise  $\alpha = 0$ . We have used that  $\bar{v}(\mathbf{r}, \mathbf{r}')$  is real and invariant with respect to all  $s$  ( $s\bar{v}s^\dagger = \bar{v}$ ). The symmetry transformation has to be applied only to the wavefunctions on the right-hand side of the equation. We do this by transforming the known  $[\tilde{M}_{\mathbf{0}I} \varphi_{\mathbf{p}_{\mathbf{k}'o'}} | \varphi_{\mathbf{p}_{\mathbf{k}'u'}}]$  to  $[\tilde{M}_{\mathbf{0}I} s \varphi_{\mathbf{p}_{\mathbf{k}'o'}} | s \varphi_{\mathbf{p}_{\mathbf{k}'u'}}]$ . We

let  $s^{-1}$  act on all quantities in [...], which corresponds to a change of integration variables. The transformation can then be performed in the space of the mixed-product basis ( $I$  index), giving  $c^{\alpha'}[(s^{-1}\tilde{M}_{\mathbf{0}I})\varphi_{\mathbf{p}_{\mathbf{k}'\alpha'}}|\varphi_{\mathbf{p}_{\mathbf{k}'\alpha'}}]$  with  $\alpha' = 1$  if  $s$  involves time reversal, otherwise  $\alpha' = 0$ .

It seems now that a very large number of such transformations have to be carried out because of the dependence of  $s = s_{\mathbf{k}}^{-1}s_{\mathbf{k}'}$  on  $\mathbf{k} \in \text{BZ}$  and  $\mathbf{k}' \in \text{BZ}$ . Note that the number of  $\mathbf{k}$  points can be very large in BSE calculations. Of course, the number of symmetry operations for different combinations of  $\mathbf{k}$  and  $\mathbf{k}'$  cannot be larger than the total set of symmetry operations. It is therefore sufficient to perform the transformation for all  $s \in S$  and store the results. The calculation of the matrix elements Eq. (29) then amounts to simple scalar products of vectors stored in memory.

### 3. Irreducible representations

One of the computationally most expensive steps in the BSE calculation is the diagonalization of the electron-hole Hamiltonian — note that the dimension of the Hamiltonian matrix is large, it grows with  $N_o N_u N_{\mathbf{k}}$  where  $N_o$ ,  $N_u$ , and  $N_{\mathbf{k}}$  are the numbers of occupied and unoccupied bands as well as the number of  $\mathbf{k}$  points. The computational cost thus grows cubically with the number of  $\mathbf{k}$  points, whereas the construction of the screened interaction  $W$  and the electron-hole Hamiltonian  $H$  exhibit only a quadratic scaling. The computation time can be reduced if the electron-hole Hamiltonian is brought into block-diagonal form. To achieve this, one has to construct a symmetry-adapted basis, in which the Hamiltonian acquires the desired form. This is indeed possible in the present case of a four-point operator, which might be surprising given the fact that group theory is usually applied in theoretical solid-state theory to mathematically less complex matrices, such as the phonon dynamical matrix or single-particle Hamiltonian.

A symmetry-adapted basis can be generated once we know the irreducible representations (irreps) of the symmetry operations (or their traces). As the name suggests, the irreps are the smallest possible matrix representations of the symmetry operations. Equation (25) defines valid representations, which, moreover, are already quite sparse, but they are *not* the smallest possible representations. In other words, the representations are reducible. So, the electron-hole products Eq. (9) are not yet the symmetry-adapted basis we are looking for. A simple way to see this is that the  $\tilde{\Gamma}$  matrix of Eq. (25) would form a  $9 \times 9$  matrix in the case of three-fold degeneracies in the occupied ( $\mathbf{k}o$ ) and unoccupied ( $\mathbf{k}u$ ) states, but the maximum irrep dimension in space groups is three. Before we explain how a symmetry-adapted basis can be constructed, we have to introduce some concepts of group theory and start by restating the great orthogonality theorem.

We restrict ourselves to linear symmetry operations

(excluding time-reversal symmetries) for simplicity. Let  $S$  be a finite symmetry group, let  $\mathcal{H}$  be a finite dimensional Hilbert space, let  $\tilde{\Gamma} = \{\tilde{\Gamma}(s)|s \in S\}$  be a unitary representation of  $S$  in  $\mathcal{H}$  [such as Eq. (25)]: For each  $s \in S$ , there is a matrix  $\tilde{\Gamma}(s)$ , and the matrices fulfill  $\tilde{\Gamma}(s) = \tilde{\Gamma}(s')\tilde{\Gamma}(s'')$  if  $s = s' \cdot s''$ . Then, group theory tells us that there exists a basis transformation that brings all representations  $\tilde{\Gamma}(s)$  into block-diagonal form

$$\tilde{\Gamma}(s) \rightarrow \Gamma(s) = \begin{pmatrix} \Gamma_1(s) & 0 & \dots & 0 \\ 0 & \Gamma_2(s) & & \vdots \\ \vdots & & \ddots & 0 \\ 0 & \dots & 0 & \Gamma_n(s) \end{pmatrix}. \quad (31)$$

Just as  $\tilde{\Gamma}$  and  $\Gamma$ , the sets  $\Gamma_m = \{\Gamma_m(s)|s \in S\}$  ( $1 \leq m \leq n$ ) are representations of the group  $S$ . The transformation is defined such that the  $\Gamma_m$  cannot be reduced any further; they are called irreducible representations (irreps). For a given  $m$ , the matrices  $\Gamma_m(s)$  have the same dimensions, they are  $1 \times 1$ ,  $2 \times 2$ , or  $3 \times 3$  matrices. Since the maximal irrep dimension is thus 3,  $n$  is of the same order of magnitude as the dimension of  $\mathcal{H}$ . On the other hand, we know from group theory that the number of distinct irreps is smaller than or equal to the number of symmetry operations [31]; hence, many of the sets  $\Gamma_m$  are identical [32].

The reader may have noticed that we use the same symbol " $\Gamma$ " on the right-hand side of Eq. (31) as in Eq. (23) for the symmetry transformation of the single-particle wavefunctions. This choice is more than a mere notational convenience. In fact, provided that the basis sets are suitably chosen, the matrices  $\Gamma_m(s)$  and  $\Gamma(s)_{\mathbf{k}n}^{\mathbf{k}'n'}$  are identical if they correspond to the same irrep.

We now re-index the  $\Gamma_m$  by  $(\mu, i)$  where  $\mu$  ( $1 \leq \mu \leq r$ ) is an index for the irrep and  $m$  ( $1 \leq i \leq n_\mu$ ) counts the  $n_\mu$  subspaces transforming according to the same irrep. Sorting  $\Gamma_{\mu,i}$  by ascending irrep index  $\mu$  gives

$$\Gamma(s) = \begin{pmatrix} \Gamma_{1,1}(s) & 0 & \dots & 0 \\ 0 & \Gamma_{1,2}(s) & & \vdots \\ \vdots & & \ddots & 0 \\ 0 & \dots & 0 & \Gamma_{r,n_r}(s) \end{pmatrix}. \quad (32)$$

By construction, the  $\Gamma_{\mu,m}(s)$  are identical for all  $m$ , so we may omit the index  $m$  in  $\Gamma_\mu(s)$ .

Now consider a linear operator  $H$  on  $\mathcal{H}$  which commutes with all  $\Gamma(s)$ . Using the decomposition into irreps, we can write  $H$  as a matrix consisting of blocks  $H_{\nu,j}^{\mu,i}$

$$H = \begin{pmatrix} H_{1,1}^{1,1} & \dots & H_{r,n_r}^{1,1} \\ \vdots & \ddots & \vdots \\ H_{1,1}^{r,n_r} & \dots & H_{r,n_r}^{r,n_r} \end{pmatrix}. \quad (33)$$

The great orthogonality theorem of group theory states that  $H_{\nu,j}^{\mu,i} = 0$  if  $\mu \neq \nu$ , i.e., the subspaces of non-equivalent irreps do not couple with each other. The

operator  $H$  is thus block-diagonal with blocks  $H_\mu$  defined on the corresponding subspaces  $\mathcal{H}_\mu$  for each irrep  $\mu$

$$H = \begin{pmatrix} H_{\mu=1} & 0 & \dots & 0 \\ 0 & H_{\mu=2} & & \vdots \\ \vdots & & \ddots & 0 \\ 0 & \dots & 0 & H_{\mu=r} \end{pmatrix}. \quad (34)$$

Furthermore, the great orthogonality theorem states that each non-zero block  $H_{\mu,j}^{\mu,i}$  is a multiple of the identity matrix. Note that  $H_\mu$  is potentially sparse but, in general, not a multiple of the identity matrix.

#### 4. Decomposition into irreps

To relate these general results of group theory to our present case, the (reducible) representation  $\tilde{\Gamma}$  of the symmetry group is given by Eq. (25), but its decomposition into irreps  $\Gamma$  is still unknown. It will not be our goal to determine the irreps explicitly. For our purpose, it will suffice to perform a decomposition of the Hilbert space  $\mathcal{H}$  into symmetry-adapted subspaces  $\mathcal{H}_\mu$ , as this already makes the electron-hole Hamiltonian block-diagonal.

There is a unique canonical decomposition into subspaces. Consider a representation  $\tilde{\Gamma}$  of the group  $S$  on the space  $\mathcal{H}$ . Consider one of the irreps, say with the index  $\mu$ . We will now construct the subspace  $\mathcal{H}_\mu$ . At first, we define the characters  $\chi_\mu(s)$  of the representation  $\Gamma_\mu$  by

$$\chi_\mu(s) = \text{Tr}[\Gamma_\mu(s)] \in \mathbb{C}. \quad (35)$$

An important property of the characters is that they are orthonormal in the sense

$$\frac{1}{|S|} \sum_s \chi_\mu^*(s) \chi_\nu(s) = \delta_{\mu\nu} \quad (36)$$

with  $|S|$  the number of elements of  $S$ . Equation (36) is also called the *little orthogonality theorem*. In the following, we only need the character tables instead of the complete irreps. Character tables are available for all space groups from the Bilbao crystallography server [33], the International Tables for Crystallography [34], or similar publications.

With the characters  $\chi_\mu(s)$ , we can now declare an operator on  $\mathcal{H}$

$$P_\mu = \frac{d_\mu}{|S|} \sum_s \chi_\mu^*(s) \tilde{\Gamma}(s) \quad (37)$$

where  $d_\mu$  is the dimension of the  $\mu$ th irrep. The operator commutes with any matrix  $\tilde{\Gamma}(t)$

$$\begin{aligned} \tilde{\Gamma}(t)^{-1} P_\mu \tilde{\Gamma}(t) &= \frac{d_\mu}{|S|} \sum_s \chi_\mu^*(s) \tilde{\Gamma}(t^{-1}st) \\ &= \frac{d_\mu}{|S|} \sum_s \chi_\mu^*(t^{-1}st) \tilde{\Gamma}(t^{-1}st) = P_\mu. \end{aligned} \quad (38)$$

Let us assume that we already know a basis set in which the reducible representations  $\tilde{\Gamma}(s)$  block-diagonalize into  $\Gamma(s)$  of Eq. (32), which would amount to replacing  $\tilde{\Gamma} \rightarrow \Gamma$  in Eq. (37). In this basis,  $P_\mu$  is also block-diagonal. In particular, we have  $(P_\mu)_{\nu j}^{\nu' i} = (P_\mu)_{\nu i}^{\nu' i} \delta_{\nu\nu'} \delta_{ij}$ . The great orthogonality theorem applies to  $P_\mu$  and tells us that each block  $(P_\mu)_{\nu,i}^{\nu,i}$  is a multiple of the identity matrix. We can determine the prefactor by taking the trace

$$\begin{aligned} \text{Tr}[(P_\mu)_{\nu,i}^{\nu,i}] &= \frac{d_\mu}{|S|} \sum_s \chi_\mu^*(s) \text{Tr}[\Gamma_{\nu,i}(s)] \\ &= \frac{d_\mu}{|S|} \sum_s \chi_\mu^*(s) \chi_\nu(s) = d_\mu \cdot \delta_{\mu\nu}. \end{aligned} \quad (39)$$

As a consequence,  $(P_\mu)_{\nu,i}^{\nu,i} = 0$  if  $\mu \neq \nu$ , otherwise it is the identity matrix. This means that  $P_\mu$  is a projection operator that projects an arbitrary function into the subspace  $\mathcal{H}_\mu$ .

A basis for  $\mathcal{H}_\mu$  can thus be obtained by applying  $P_\mu$  of Eq. (37) to a complete set of vectors. Such a set is simply given by  $(1,0,\dots,0)$ ,  $(0,1,\dots,0)$ , etc.; each unit vector corresponds to one of the product basis functions Eq. (9). Note that the resulting set of the projected functions is highly linearly dependent, in general. Many of the functions will just vanish. Many of them will be identical. We use singular value decomposition to obtain an orthonormal basis  $\{\mathbf{v}_{\mu,k}\}_{k \leq n_\mu \cdot d_\mu}$ . It may appear computationally costly to apply the projector  $P_\mu$  in the product basis space given the large dimensionality of this space. However, the action of  $P_\mu$  on a particular product function  $\varphi_{\mathbf{k}u}(\mathbf{r}\sigma)\varphi_{\mathbf{k}o}^*(\mathbf{r}'\sigma')$  acts only within the space of the so-called *orbit* associated with that function: the orbit is the set of all product functions obtained by applying the symmetry operations to  $\varphi_{\mathbf{k}u}(\mathbf{r}\sigma)\varphi_{\mathbf{k}o}^*(\mathbf{r}'\sigma')$ . The orbit consists of all product basis function, whose constituent occupied and unoccupied states are energy degenerate to  $\varphi_{\mathbf{k}u}$  and  $\varphi_{\mathbf{k}o}$ . Each orbit can thus be regarded as an equivalence class that groups together all degenerate product functions. The orbit dimension is much smaller than the product-basis dimension and is at most  $|S|d_{\max}^2$ , where  $d_{\max}$  is the maximal degree of degeneracy;  $d_{\max} = 3$  is the maximum value among all space groups. Specifically, the size of  $\mathcal{H}_{[\mathbf{k}uo]}$  does not scale with the size of the  $\mathbf{k}$  point grid or the number of bands that define the two-particle basis.

By repeating the above procedure for all irrep classes, we obtain orthonormal symmetry-adapted basis sets for all irreps. The subspaces  $\mathcal{H}_\mu$  themselves are orthogonal to each other, as well, so that we finally obtain an orthogonal basis transformation matrix

$$U = \begin{pmatrix} \mathbf{v}_{1,1}^* \\ \dots \\ \mathbf{v}_{r,n_r d_r}^* \end{pmatrix} \quad (40)$$

which decomposes our representation  $\tilde{\Gamma}$  into the irreps. The transformation  $U^\dagger H U$  then yields the block-diagonal form of the electron-hole Hamiltonian of Eq. (34).

The transformation  $U^\dagger H U$  can be performed "irreversible",  $U_\mu^\dagger H U_\mu$ . Furthermore, the vectors  $\{\mathbf{v}_{\mu,k}\}$  have maximally  $|S|d_{\max}^2$  non-zero components. This upper bound on the number of non-zero components does not increase with the system size or the  $\mathbf{k}$  grid. The transformation matrix  $U$  is therefore sparse.

## D. Symmetry-reduced BSE Hamiltonian

### 1. Optical absorption spectrum

Diagonalizing the  $r$  blocks  $U_\mu^\dagger H U_\mu$  with a parallel solver gives the full set of eigensolutions of  $H$ , categorized into irreps. Assuming that all  $r$  blocks have the same size, one would estimate a computational speedup of  $r^2$  with respect to the diagonalization of the full matrix  $H$ :  $r$  blocks, each diagonalization costs  $1/r^3$  relative to the full matrix. However, as discussed below, not all irreps are relevant for optical absorption. In fact, in the present examples, we find that only one of the irreps contributes to the absorption spectrum, while all others do not. The estimated speedup for the diagonalization is therefore as large as  $r^3$ .

Each of the obtained eigenfunctions belongs to a single irrep, which guarantees that their symmetry is fully preserved and no averaging step is needed in the visualization.

Other approaches that circumvent the diagonalization of the electron-hole Hamiltonian, for example, the time-evolution approach [35] or the Lanczos-Haydock method [36], also benefit from the sparse block-diagonal form of  $H$ . For example, in the case of the Lanczos-Haydock method, the final absorption spectrum is simply given by the sum of the "Lanczos-Haydock spectra" calculated for each contributing block separately. Here, too, only one irrep may need to be taken into account.

Equation (3) together with Eq. (4) yields the macroscopic dielectric function  $\epsilon_M(\omega)$ , whose imaginary part gives the optical absorption spectrum. The eigensolutions enter Eq. (4) with the eigenvalues  $\Omega_\lambda$  and eigenvectors  $A_{\mathbf{k}u\sigma}^\lambda$ . To be more precise, only those eigenvectors contribute to the absorption spectrum for which Eq. (5) is non-zero. Let us write Eq. (5) as  $\sum_{\mathbf{k}u\sigma} A_{\mathbf{k}u\sigma}^\lambda B_{\mathbf{k}u\sigma}$  and, expressed in the symmetry-adapted basis, as  $\sum_k A_{\mu k}^\lambda B_{\mu k}$ .

It turns out that  $B_{\mu k} = 0$  ( $1 \leq k \leq n_\mu$ ) for most irreps  $\mu$ . In fact, we have found it to vanish for all but one irrep in our calculations. This means that only one of the Hamiltonian blocks  $H_\mu$  is relevant for the optical absorption spectrum (although, for certain choices of the polarization vector  $\mathbf{q}$  more than one — but maximally three — irrep blocks may be relevant). As already pointed out in the previous paragraph, this significantly reduces the computational cost of the diagonalization.

### 2. Excitonic energies and loss spectrum

So far, we have discussed the poles of the optical absorption spectrum or macroscopic dielectric function  $\epsilon_M(\omega)$ , which are given by the eigenvalues of the electron-hole Hamiltonian Eq. (7) corresponding to transversal excitons. Another set of eigenvalues, the longitudinal excitons, form the pole structure of the *inverse* macroscopic dielectric function  $\epsilon_M^{-1}(\omega)$ . Its imaginary part is proportional to the electron-energy loss spectrum [37]. A similar derivation as the one leading to Eq. (7), gives rise to an eigenvalue equation for  $\epsilon_M^{-1}(\omega)$  identical in structure to Eq. (7) but with the important difference that the modified Coulomb potential  $\bar{v}$  should be replaced by the real, unmodified Coulomb potential  $v$ .

As a consequence, a term arising from the Coulomb divergence eliminated for  $\bar{v}$  has to be added to Eq. (7) to get the Hamiltonian for the electron-energy loss spectrum. This term can be extracted from Eq. (12) expressed in a plane-wave basis instead of the mixed basis  $\{M_{\mathbf{q}\mathbf{r}}(\mathbf{r})\}$ . The Coulomb matrix is then diagonal, and the double sum over  $IJ$  becomes a single sum over  $\mathbf{G}$ . The desired term is the one for  $\mathbf{G} = \mathbf{0}$ , for which the Coulomb matrix element diverges as  $v_{\mathbf{q}} \stackrel{\mathbf{q} \rightarrow \mathbf{0}}{\sim} 4\pi/q^2$ . Luckily, the other two terms are linear in  $q$ ,

$$\frac{1}{\sqrt{V_{\text{uc}}}} \lim_{q \rightarrow 0} \langle e^{i\mathbf{q}\mathbf{r}} \varphi_{\mathbf{k}n} | \varphi_{\mathbf{k}+\mathbf{q}m} \rangle = \frac{1}{\sqrt{V_{\text{uc}}}} \mathbf{q} \frac{\langle \varphi_{\mathbf{k}n} | -i\nabla | \varphi_{\mathbf{k}m} \rangle}{\epsilon_{\mathbf{k}m}^0 - \epsilon_{\mathbf{k}n}^0}, \quad (41)$$

so that the  $\mathbf{G} = \mathbf{0}$  term is finite

$$\begin{aligned} v_{\mathbf{k}u,\mathbf{k}'\sigma';\mathbf{k}o,\mathbf{k}'u'}^{\text{div}} &= \frac{4\pi}{N_{\mathbf{k}}V} \frac{\langle \varphi_{\mathbf{k}u} | -i(\hat{\mathbf{q}}\nabla) | \varphi_{\mathbf{k}o} \rangle}{\epsilon_{\mathbf{k}u}^0 - \epsilon_{\mathbf{k}o}^0} \\ &\times \frac{\langle \varphi_{\mathbf{k}'\sigma'} | -i(\hat{\mathbf{q}}\nabla) | \varphi_{\mathbf{k}'u'} \rangle}{\epsilon_{\mathbf{k}'u'}^0 - \epsilon_{\mathbf{k}'\sigma'}^0} \\ &= \frac{4\pi}{N_{\mathbf{k}}V} B_{\mathbf{k}u\sigma}^* B_{\mathbf{k}'u'\sigma'} \end{aligned} \quad (42)$$

with  $\hat{\mathbf{q}} = \mathbf{q}/q$ , the polarization direction of the incoming beam of light. On the right-hand side, we encounter again the quantity defined in Eq. (6).

Equation (42), the term to be added to Eq. (7), will, in general, affect all matrix elements. It seems that this gives rise to yet another eigenvalue equation of the same dimensions, which would double the cost of solving the BSE (if we want the eigenvalue spectrum of both the optical absorption spectrum and the excitonic eigenvalue spectrum). Fortunately, transforming the resulting modified electron-hole Hamiltonian  $H'$  to the eigenbasis of the original (unmodified) Hamiltonian  $H$  recovers a classical problem of linear algebra with a well-known solution. The resulting secular equation turns out to be the condition  $\text{Re}[\epsilon_M(\Omega'_\xi)] = 0$ , giving the eigenvalues  $\Omega'_\xi$  of  $H'$  as the poles of the inverse macroscopic dielectric function  $\epsilon_M^{-1}(\omega)$ .

Before we discuss the secular equation, we first have a closer look at the modified eigenvalue problem. The transformation to the eigenspace of  $H$  yields  $v_{\lambda\lambda'}^{\text{div}} =$

$4\pi/(N_k V)B_\lambda^* B_\lambda$ . If one of the  $B_\lambda$ , say for the  $\lambda$ th eigenvector, vanishes, then the  $\lambda$ th row and  $\lambda$ th column of  $H'$  will be identical to the ones of  $H$ . Thus, the  $\lambda$ th eigensolution of  $H$  will also be an eigensolution of  $H'$  (with zero coupling to light, i.e., a dark exciton). Such eigenvectors can thus be eliminated from the eigenvector basis. For the same reason, only the eigensolutions of the irrep(s) relevant for the optical absorption spectrum (see previous paragraph) need to be taken into account. Finally, given a set of  $n$  degenerate eigensolutions of  $H$ , we can always make a unitary transformation among them such that only one of the  $B_\lambda$  is non-zero and the others vanish. The corresponding eigensolutions  $\{\Omega_\lambda, A^\lambda\}$  for which  $B_\lambda = 0$  are then eigensolutions to  $H'$ , too, and can be eliminated from the eigenvalue problem of  $H'$ . We thus end up with an eigenvalue problem, in which all eigenvalues can be assumed to be non-degenerate.

Applying the matrix determinant lemma to the characteristic equation of  $H'$  in the eigenspace of  $H$ ,  $\det[H - \Omega' I + 4\pi/(N_k V)\mathbf{B}^* \mathbf{B}^T] = 0$  with the identity matrix  $I$ , leads to the secular equation

$$1 - \frac{4\pi}{N_k V} \sum_\lambda \frac{|B_\lambda|^2}{\Omega' - \Omega_\lambda} = 0, \quad (43)$$

which corresponds to the condition  $\text{Re}[\varepsilon_M(\Omega'_\xi)] = 0$  for the eigenvalues  $\Omega'_\xi$  of the modified Hamiltonian. The function on the left-hand side has poles at the unperturbed eigenvalues  $\Omega_\lambda$ . Between two consecutive eigenvalues,  $\Omega_\lambda$  and  $\Omega_{\lambda+1}$ , the function is strictly monotonically decreasing so that there is a solution  $\Omega'_\xi$  between each pair of unperturbed eigensolutions. There is an additional solution above the highest unperturbed eigenvalue. The lowest  $\Omega'_\xi$  (with a non-zero oscillator strength) is thus strictly higher than the lowest unperturbed eigenvalue  $\Omega_\lambda$ . Numerically, the nodes can be found efficiently, e.g., by interval nesting or the Newton method. We use the LAPACK routine DLASD4, which after suitable preparation of the input data, can be used for the purpose of solving the secular Equation (43).

The corresponding eigenvectors  $\mathbf{A}'^\xi$  fulfill

$$\left( H + \frac{4\pi}{N_k V} \mathbf{B}^* \mathbf{B}^T \right) \mathbf{A}'^\xi = \Omega'_\xi \mathbf{A}'^\xi, \quad (44)$$

from which we can derive the closed form

$$A'_\lambda{}^\xi = \frac{B_\lambda^*}{\Omega_\lambda - \Omega'_\xi} \left( -\frac{4\pi}{N_k V} \mathbf{B}^T \mathbf{A}'^\xi \right) \quad (45)$$

for its components in the eigenbasis of  $H$ . The bracket on the right-hand side is unknown but non-zero by construction. Since eigenvectors are defined only up to a factor, this factor is irrelevant, and the eigenvector is fully defined by Eq. (45). Multiplying with  $A'_\lambda{}^\xi$  and summing over  $\lambda$  identifies Eq. (45) simply as the condition  $\text{Re}[\varepsilon_M^{-1}(\Omega_\lambda)] = 0$ , the companion condition to  $\text{Re}[\varepsilon_M(\Omega'_\xi)] = 0$ : The poles of the macroscopic dielectric function are the nodes of its inverse  $\varepsilon_M^{-1}(\omega)$ . Calculating

the eigenvalue spectrum from the secular Eq. (43) and the eigenvectors from Eq. (45) takes negligible computation time.

## E. Parallel storage

Due to the quadratic scaling of the number of product basis functions with respect to the system size and its cubic scaling with respect to the number of  $\mathbf{k}$  points, it is essential to parallelize the code in order to treat large systems and/or achieve high accuracy. In particular, the large size of the electron-hole Hamiltonian requires the matrix to be stored in parallel across multiple compute nodes, since the limited memory of a single node is quickly exhausted.

We use a two-step process. In the first step, the Hamiltonian  $H$  is calculated in the standard two-particle product basis. When  $H$  is complete, it is transformed to the symmetry-adapted basis in a second step. Both matrices are stored in distributed memory, which requires a suitable data distribution strategy using MPI as described in the following.

As we use the Tamm-Dancoff approximation, the Hamiltonian matrix  $H$  is Hermitian, and we can afford to just store its upper triangle in the first step. The storage of this upper triangle is evenly distributed across the compute nodes. Each node keeps its part in shared memory (MPI 3.1), i.e., shared among the processes on that node: All processes of the node can access this memory by load/store operations as if it were an array allocated by the process itself.

The calculation of the matrix elements is parallelized over the processes. All processes independently calculate matrix elements with a minimum of communication between the processes (and without calculating any element twice). However, due to the usage of symmetries in the calculation of the matrix elements, see Sec. III C 1, the matrix elements calculated by a given process are not contiguous in memory. It is therefore not possible for the processes to calculate only the matrix elements that are stored in the memory of the local node. All processes eventually need to send their values to all nodes (except their own).

Here, we use the following strategy: A given process writes the matrix elements with fast store operations either to the (node-)local part of the matrix or to a buffer array. (Each process has  $N - 1$  buffer arrays, where  $N$  is the number of nodes.) There is an outer loop in the calculation of the BSE direct and exchange matrix elements, namely over the  $\mathbf{k}$  points (of the irreducible wedge) in the former [corresponding to the contribution of  $W(\mathbf{k})$ ] and over the processes in the latter. At the end of each loop iteration, several send-receive (MPI Sendrecv) operations are executed to transmit buffer data to the corresponding remote nodes, where a local process receives it and writes it to the local portion of the matrix stored on that node. In this way, the communication always transfers

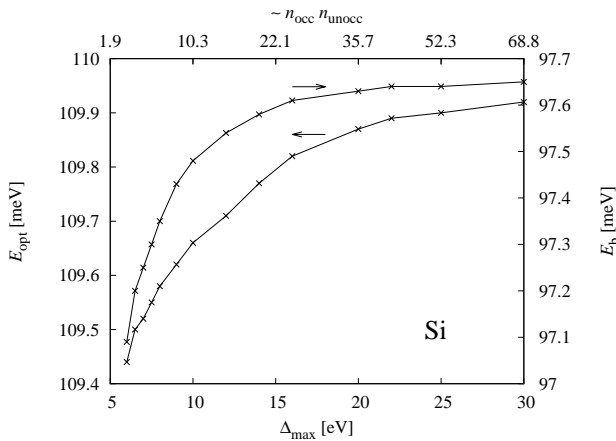


FIG. 1. Convergence of  $E_{\text{opt}}$  and  $E_b$  with respect to the product-basis cutoff parameter  $\Delta_{\text{max}}$ . The upper  $x$  axis shows the average product  $n_{\text{occ}}n_{\text{unocc}}$  (see text).

contiguous memory arrays (the buffer arrays) and the (non-contiguous) writing to the matrix is performed by fast store operations. The communication overhead is well below the computation time of the matrix elements.

In the second step,  $H$  is transformed to the symmetry-adapted basis using the (sparse) transformation matrix Eq. (40). The result of the transformation is stored in block-cyclic form as required by the parallel linear-algebra libraries ScaLAPACK [38] or ELPA [39, 40]. Specifically, the right-multiplication of the  $U$  matrix is calculated in a round-robin fashion giving, in each iteration and process, a very thin matrix with  $b$  columns where  $b$  is the chosen block size, typically 64, 96, or 128. The left-multiplication of  $U^\dagger$  is then done by the same process in chunks of  $b$  rows so that, in each step, the result is a complete  $b \times b$  block, which is then sent to the process that owns that block (according to the block-cyclic distribution). Before calculating the next block, each process receives its own blocks from other processes. In this way, the transformed Hamiltonian is immediately stored in block-cyclic form and can be passed to the parallel linear algebra library. In this step, the communication overhead can be significant for very large matrix sizes, but it is still far below the total computation time.

#### IV. RESULTS AND DISCUSSION

To verify the code and to demonstrate the speedup achieved, we show results for bulk silicon, lithium fluoride, and molybdenum disulfide. For these materials, there are numerous BSE studies in the literature for comparison. For each material, we show the convergence of the lowest peaks of the optical absorption ( $E_{\text{opt}}$ ) and the electron-energy loss spectra ( $E_b$ ) relative to the conduction band minimum. They correspond to the transversal and longitudinal exciton binding energies, respectively.

The non-interacting reference system is obtained from a standard Kohn-Sham DFT calculation with the

Perdew-Burke-Ernzerhof functional [41]. Since the focus here is on the numerical method rather than the results (which are well established in the literature) and to facilitate reproducibility of the results, we apply a simple scissors shift to open the band gap to (approximately) the  $GW$  gap, instead of performing a  $GW$  calculation beforehand.

We first turn to bulk silicon. The experimental lattice constant of  $5.43 \text{ \AA}$  is used. The ground-state calculation is carried out with a  $16 \times 16 \times 16$   $\mathbf{k}$ -point grid. Further computational parameters are the reciprocal cutoff radius of  $4.0 \text{ bohr}^{-1}$  and an  $l$  cutoff of 8. The MT radius is  $2.15 \text{ bohr}$ . The Kohn-Sham DFT direct ( $\Gamma - \Gamma$ ),  $\Gamma - X$ , and fundamental band gaps of  $2.56 \text{ eV}$ ,  $0.71 \text{ eV}$ , and  $0.57 \text{ eV}$ , respectively, underestimate the experimental gaps. To align the direct band gap approximately with the experimental one ( $3.3 \text{ eV}$  [42]), we apply a scissor operator in the calculation of the electron-hole Hamiltonian that uniformly shifts the conduction bands up by  $0.75 \text{ eV}$ . A total of 100 bands are included in the calculation of the screened interaction. Both the bare and the screened interaction ( $v$  and  $W$ ) are expanded in the mixed basis with a reciprocal cutoff radius of  $3.0 \text{ bohr}^{-1}$  and an  $l$  cutoff of 4. We use the formalism of the random-phase approximation for  $W$  without resorting to a plasmon-pole model or similar simplifications.

Instead of specifying the numbers of occupied and unoccupied states from which the product basis is constructed, we employ an energy cutoff  $\Delta_{\text{max}}$  and include all products Eq. 9 into the basis for which  $\epsilon_{\mathbf{k}u}^0 - \epsilon_{\mathbf{k}o}^0 < \Delta_{\text{max}}$ . The advantage is that there is only one parameter to converge (instead of two). Another advantage is that degenerate states are always either fully included in the product basis or excluded. This avoids cutting degenerate subspaces, which would otherwise result in symmetry breaking.

Figure 1 shows the convergence of  $E_{\text{opt}}$  and  $E_b$  with respect to  $\Delta_{\text{max}}$  calculated with an  $8 \times 8 \times 8$   $\mathbf{k}$ -point sampling. The upper  $x$  axis further indicates the quantity  $n_{\text{occ}}n_{\text{unocc}}$  averaged over the  $\mathbf{k}$  grid. To be more precise, this quantity corresponds to the number of product basis function Eq. (9) divided by the number of  $\mathbf{k}$  points ( $8^3 = 512$  in this case). It provides a link to the usual product-basis specification in literature, which is expressed in terms of  $n_{\text{occ}}$  and  $n_{\text{unocc}}$  (together with the  $\mathbf{k}$  grid). For example, if  $n_{\text{occ}} = n_{\text{unocc}} = 2$ , then  $n_{\text{occ}}n_{\text{unocc}} = 4$  should be compared to the values given on the upper  $x$  axis of the diagram. We observe a very fast convergence with respect to  $\Delta_{\text{max}}$ . Both  $y$  axes show a tiny energy range of less than  $1 \text{ meV}$ . We use  $\Delta_{\text{max}} = 7.5 \text{ eV}$  for our calculations in the following, which corresponds to  $n_{\text{occ}}n_{\text{unocc}} \approx 5.6$ .

The number of  $\mathbf{k}$  points is an important convergence parameter for BSE calculations. It is known that exciton binding energies converge slowly with the  $\mathbf{k}$  grid. On the other hand, the number of  $\mathbf{k}$  points strongly impacts the computational cost. The diagonalization of the BSE electron-hole Hamiltonian scales as  $n^9$  for an  $n \times n \times n$   $k$ -

Si				
$\mathbf{k}$ grid	full dim	block dim	$E_{\text{opt}}$ [meV]	$E_b$ [meV]
$6 \times 6 \times 6$	1 284	264	137.6	115.3
$8 \times 8 \times 8$	2 868	561	109.6	97.3
$12 \times 12 \times 12$	9 978	1 917	73.2	67.9
$16 \times 16 \times 16$	22 902	4 380	54.4	51.4
$20 \times 20 \times 20$	45 344	8 637	43.7	41.5
$24 \times 24 \times 24$	78 990	14 988	36.8	35.1
$30 \times 30 \times 30$	153 246	28 998	30.4	28.8
$36 \times 36 \times 36$	264 194	49 905	26.5	24.9
$42 \times 42 \times 42$	418 688	79 002	24.3	22.3
$50 \times 50 \times 50$	707 756	133 401	22.9	20.4
$60 \times 60 \times 60$	1 220 864	229 887	22.5	19.5
exp. [43]	—	—	15	—

TABLE I. BSE calculations of silicon for different  $\mathbf{k}$ -point sets. We report the number of rows (columns) of the full electron-hole Hamiltonian (full dim) as well as the number of rows (columns) of the symmetry-reduced Hamiltonian block (block dim). The last two columns contain the exciton binding energies appearing as the lowest peaks in the absorption spectrum ( $E_{\text{opt}}$ ) and the electron-energy loss spectrum ( $E_b$ ) as well as the experimental value.

point sampling. Furthermore, the construction of the screened interaction scales as  $n^6$ . Since DFT calculations usually converge quickly with the  $\mathbf{k}$  grid, we store the self-consistent effective potential obtained with the  $16 \times 16 \times 16$  set on harddisc and use it for all BSE calculations. Each calculation starts with the generation of the Kohn-Sham eigensolutions  $\{\varphi_{\mathbf{k}n}, \epsilon_{\mathbf{k}n}\}$  on the respective  $\mathbf{k}$  grid. The screened interaction is calculated and expanded in the mixed basis, then projected onto the BSE product basis according to Eq. 8 yielding the direct term of Eq. 7. Likewise, the exchange term of Eq. 7 is calculated with the corresponding mixed-basis expansion of the bare interaction. The so-constructed electron-hole Hamiltonian is transformed to the symmetry-reduced Hamiltonian according to Sec. III C 4, which is then diagonalized using a standard parallel diagonalizer (ScaLAPACK or ELPA).

Table I shows the  $\mathbf{k}$  convergence of the transversal and longitudinal exciton binding energies relevant for the absorption ( $E_{\text{opt}}$ ) and EEL spectrum ( $E_b$ ). The matrix dimensions of the full Hamiltonian and the symmetry-reduced Hamiltonian are shown in the second and third column, respectively. The latter amounts to about 20% of the former. Given that numerical diagonalization scales cubically with the matrix dimension, this would result in an acceleration factor of 125 for this step. Both  $E_{\text{opt}}$  and  $E_b$  converge slowly with respect to the  $\mathbf{k}$  grid.

Figure 2 shows the behavior of  $E_{\text{opt}}$  and  $E_b$  with respect to the  $\mathbf{k}$  grid  $n \times n \times n$  as a function of  $1/n$ . The energies do not exhibit a clear analytic behavior for increasingly dense  $\mathbf{k}$  meshes that would allow for an extrapolation to the infinite-mesh limit. We therefore consider the values at  $60 \times 60 \times 60$  to be our best estimates. In fact, the curves level off at this point indicating that the values are already close to the infinite-mesh limit.

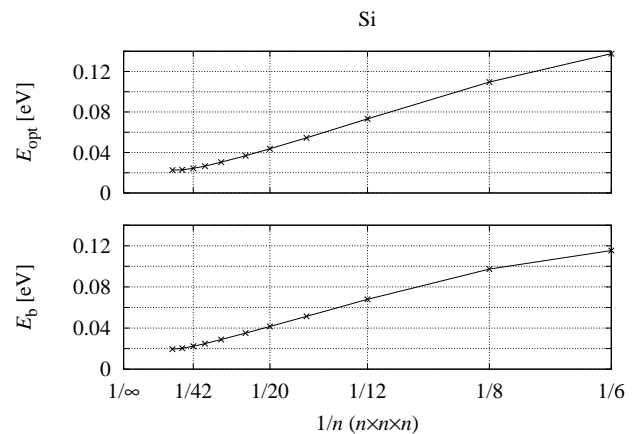


FIG. 2. Convergence of  $E_{\text{opt}}$  and  $E_b$  with respect to the  $\mathbf{k}$  grid  $n \times n \times n$  as a function of  $1/n$  for Si.

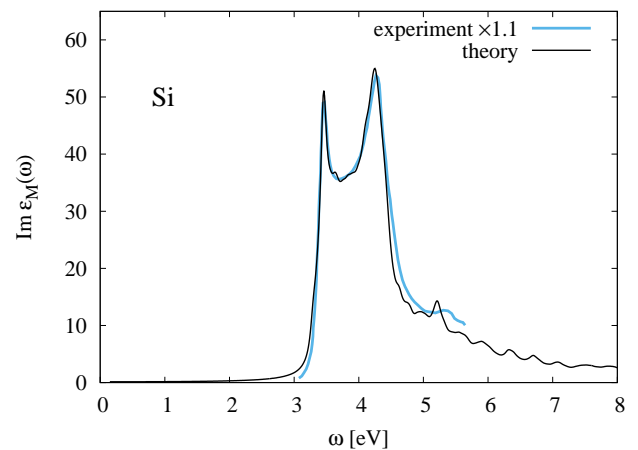


FIG. 3. Comparison of the theoretical ( $60 \times 60 \times 60$ ) and experimental absorption spectrum [46] for Si. The experimental spectrum was vertically scaled by a factor of 1.1.

The first peak  $E_{\text{opt}} = 22.5$  meV of the optical absorption spectrum still overestimates the experimental value of 15 meV [43] but is closer to experiment than previous ab initio BSE binding energies [44]. The result of 22.5 meV is close to the recently published exciton binding energy of 24 meV calculated based on a non-uniform Brillouin-zone sampling scheme [45].

Figure 3 presents a comparison of the theoretical absorption spectrum  $\text{Im}\epsilon_M(\omega)$  calculated with a  $60 \times 60 \times 60$   $\mathbf{k}$  mesh to the experimental absorption spectrum from Ref. 46. The experimental spectrum was vertically scaled by a factor of 1.1. The shapes of the two spectra agree very well. Both spectra also exhibit a small shoulder at roughly the same energy around 5.2 eV. It should be noted that the fact that the peaks align so well horizontally is due to the choice of the scissor operator. For example, a scissor operator of 0.80 eV would shift the theoretical spectrum by 50 meV to the right.

The second test material is lithium fluoride. We employ the experimental lattice constant of 4.026 Å. The DFT calculation is carried out with a reciprocal cutoff

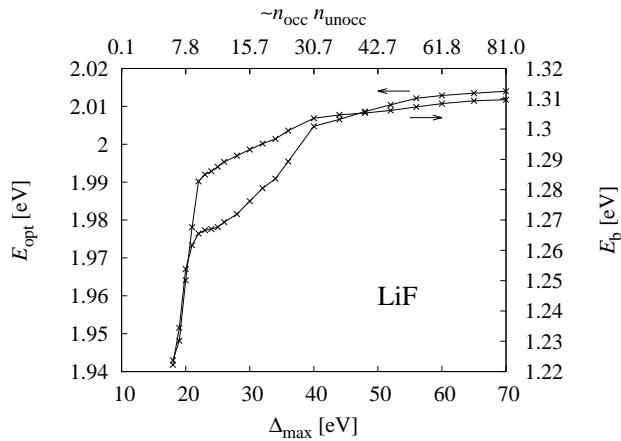


FIG. 4. Same as Fig. 1 for LiF.

radius of  $4.4 \text{ bohr}^{-1}$  and  $l$  cutoff values of 9 and 7 for Li and F, respectively. The  $1s$  core state of lithium is treated as a semicore state with a local orbital. We also add  $s$  and  $p$  local orbitals to the fluorine atom at high energies, to improve the description of high-lying states. The Kohn-Sham band gap is  $9.05 \text{ eV}$ . To account for the underestimation of the band gap in DFT, we will employ a scissor shift as in the case of Si. However, as the experimental value of the direct band gap is not known accurately, we will determine the scissor operator later by aligning the theoretical and experimental absorption spectra. The band summations for the polarization function comprise all available bands (160-190 bands). The mixed basis is constructed with a reciprocal cutoff radius of  $3.3 \text{ bohr}^{-1}$  and  $l$  cutoff values of 5 and 4 for Li and F, respectively.

Figure 4 shows the convergence of  $E_{\text{opt}}$  and  $E_b$  with respect to  $\Delta_{\text{max}}$  for LiF. Due to the large band gap, the screening is weak giving rise to a strong interaction between the electron and the hole. The exciton binding energy is therefore much larger than in the case of silicon. The convergence is slower than for Si, as is evident from the markedly different energy scales:  $100 \text{ meV}$  for LiF vs. less than  $1 \text{ meV}$  for Si. As a consequence, we have to choose a much larger  $\Delta_{\text{max}}$  parameter than in the Si case. We employ  $\Delta_{\text{max}} = 50 \text{ eV}$ , which corresponds to  $n_{\text{occ}}n_{\text{unocc}} \approx 42.7 \approx 6 \times 7$ .

The  $\mathbf{k}$  convergence of  $E_{\text{opt}}$  and  $E_b$  is presented in Table II. The densest  $\mathbf{k}$ -point set is  $36 \times 36 \times 36$ . The number of product basis functions for this  $\mathbf{k}$ -point set reaches nearly 2 million. The symmetry-reduced Hamiltonian, however, has a much smaller dimension of only 0.38 million. Diagonalizing a matrix of this size is feasible on a modern supercomputer. Overall, we see a slower convergence than in the case of Si, but due to the larger energies, a faster relative convergence. The difference between  $E_{\text{opt}}$  and  $E_b$  is quite large and quickly converges to about  $725 \text{ meV}$ .

Figure 5 presents a graphical representation of the  $\mathbf{k}$ -mesh convergence. In contrast to Si, linear extrapolation

LiF				
$\mathbf{k}$ grid	full dim	block dim	$E_{\text{opt}}$ [eV]	$E_b$ [eV]
$6 \times 6 \times 6$	9 200	1 860	1 983	1 350
$8 \times 8 \times 8$	21 838	4 338	2 009	1 306
$12 \times 12 \times 12$	73 426	14 313	2 066	1 344
$16 \times 16 \times 16$	174 224	33 636	2 099	1 375
$20 \times 20 \times 20$	339 984	65 253	2 120	1 395
$24 \times 24 \times 24$	587 680	112 362	2 133	1 408
$30 \times 30 \times 30$	1 147 662	218 580	2 147	1 422
$36 \times 36 \times 36$	1 982 862	376 662	2 157	1 432
$\infty$	$\infty$	$\infty$	2 202	1 475
exp. [47]	—	—	2 090	—
exp. [48]	—	—	1 900	—

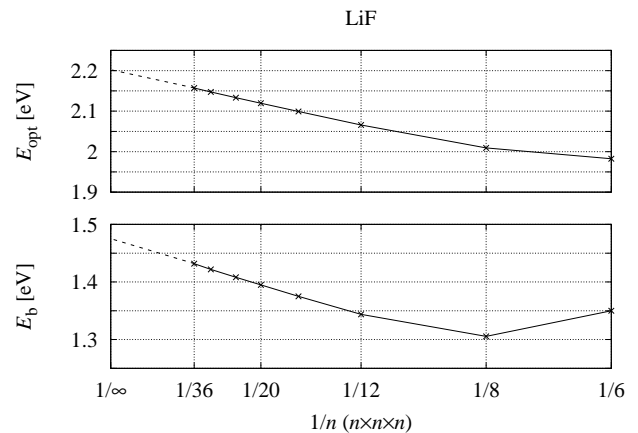
TABLE II. Same as Table I for lithium fluoride. The row marked with  $\infty$  reports the extrapolated exciton binding energies.

FIG. 5. Same as Fig. 2 for LiF. The linear extrapolation to the infinite-mesh limit is indicated by dashed lines.

to the infinite-mesh limit is possible and yields the values given in the row marked " $\infty$ " in Table II. The extrapolated exciton binding energy  $E_{\text{opt}}$  is relatively close to the experimental value of  $2.09 \text{ eV}$  [47]. It should be noted, however, that  $E_{\text{opt}}$  is not known accurately in experiment [48]. The experimental value of  $2.09 \text{ eV}$  might thus be a bit misleading in terms of its apparent accuracy. Theoretical studies [8, 49, 50] have consistently reported smaller  $E_{\text{opt}}$  between  $1.5$  and  $1.6 \text{ eV}$ . However, a recent BSE study reported  $2.05 \text{ eV}$  using a  $16 \times 16 \times 16$  grid, close to our value of  $2.10 \text{ eV}$  with this grid. The  $\sim 0.6 \text{ eV}$  variance between theoretical values calls for a comparative study of the various implementations in order to examine the numerical differences in detail. Rohlfing and Louie [8] report  $0.5 \text{ eV}$  for the difference  $E_{\text{opt}} - E_b$  in reasonable agreement to our value.

Figure 6 presents a comparison between the theoretical absorption spectrum calculated with a  $36 \times 36 \times 36$  grid and the experimental absorption spectrum of Ref. 51, in which the two components of the refractive index  $N(\omega) = n(\omega) + i\kappa(\omega) = \sqrt{\epsilon_M(\omega)}$  are plotted and tabulated. We thus plotted  $\text{Im}N^2(\omega)$  as the experimental absorption spectrum. To align the two spectra, we

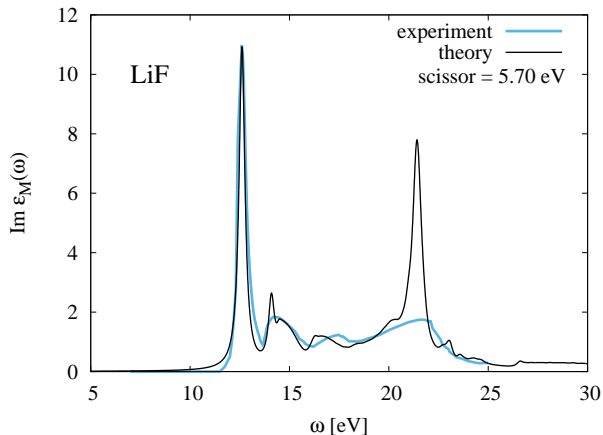


FIG. 6. Comparison of the theoretical ( $36 \times 36 \times 36$ ) and experimental absorption spectrum [51] for LiF.

employed a scissor operator of 5.7 eV and a Lorentzian broadening parameter of 0.18 eV to the theoretical spectrum. The sharp  $1s$  exciton peak at 12.6 eV is well reproduced. There is a broader peak around 14.5 eV, with a similar shape in the two spectra. A shallow feature at 17 eV appears at somewhat lower energy in the theoretical spectrum. A sharp peak in the theoretical spectrum at 21.4 eV appears as a broad feature in the experimental spectrum. Both spectra drop off at around 22.2 eV in a similar manner.

As a final test system, we consider bulk  $\text{MoS}_2$ , which crystallizes in a hexagonal lattice with layers stacked along the  $z$  axis. We employ the lattice constants  $a = 3.16$  Å and  $c = 12.3$  Å and an internal parameter of 0.623. The DFT calculation is carried out with the PBE functional on a  $12 \times 12 \times 3$   $\mathbf{k}$ -point mesh. The MT radii for Mo and S are 2.41 bohr and 1.99 bohr, respectively. The reciprocal cutoff radius is set to 4.00 bohr $^{-1}$ . The cutoff values for the  $l$  quantum number are 9 for Mo and 8 for S. The Mo  $4s$  and  $4p$  states are described by local orbitals. Spin-orbit coupling is included consistently throughout the DFT and BSE calculations. The direct and indirect DFT bandgaps are 1.64 eV and 0.87 eV, respectively, which underestimate the experimental gaps by a few 100 meV. We will later employ a scissor operator as in the case of LiF. The band summations for the polarization function include 200 bands, ensuring that the exciton binding energies are converged to within 1 meV with respect to this parameter. For the mixed basis, we employ a reciprocal cutoff radius of 3.0 bohr $^{-1}$  and  $l$  cutoff values of 5 and 4 for Mo and S, respectively.

Figure 7 shows the convergence of the exciton binding energies  $E_{\text{opt}}$  and  $E_b$  as a function of the product-basis cutoff energy  $\Delta_{\text{max}}$ . The convergence is faster than in LiF but not as fast as in the case Si. For  $E_{\text{opt}}$  convergence to within 1 meV is reached at around  $\Delta_{\text{max}} = 4$  eV, whereas  $E_b$  converges a bit more slowly. Since we are mostly interested in the optical spectra, we adopt  $\Delta_{\text{max}} = 4$  eV for the BSE calculations, which cor-

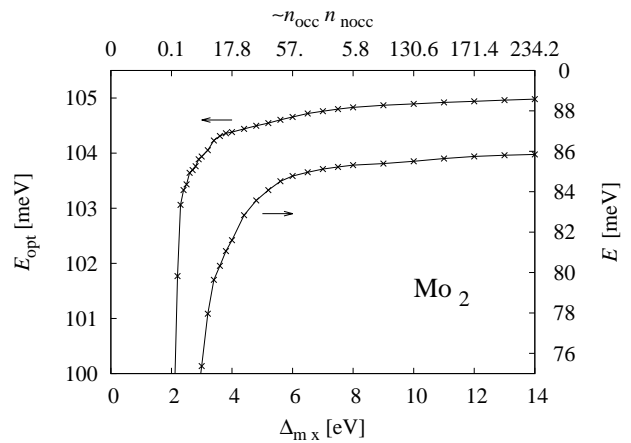


FIG. 7. Same as Fig. 1 for bulk  $\text{MoS}_2$ .

MoS <sub>2</sub>					
$\mathbf{k}$ grid	full dim	block dim	$E_{\text{opt}}$ [meV]	$E_b$ [meV]	
$6 \times 6 \times 3$	7 892	1 330	290	256	
$12 \times 12 \times 3$	30 980	5 178	134	118	
$18 \times 18 \times 3$	68 996	11 514	95	84	
$24 \times 24 \times 3$	123 644	20 622	81	70	
$30 \times 30 \times 3$	193 028	32 186	76	65	
$42 \times 42 \times 3$	378 284	63 062	76	64	
exp. [52]	—	—	50	—	
exp. [53]	—	—	87	—	
exp. [54]	—	—	84	—	

TABLE III. Same as Table I for bulk  $\text{MoS}_2$ .

responds to  $n_{\text{occ}}n_{\text{unocc}} = 17.8$ ; i.e., typically four occupied and four unoccupied bands are included in the product basis.

Table III shows the convergence of the exciton binding energies  $E_{\text{opt}}$  and  $E_b$  with respect to the  $\mathbf{k}$ -point sampling. As in the case of Si, the convergence is slow, in particular for the in-plane  $\mathbf{k}$ -point set, whereas the out-of-plane  $\mathbf{k}$  convergence is faster (see Fig. 8). The resulting excitonic binding energy of 76 meV is in good agreement to the experimental values 50 meV [52], 87 meV [53] and 84 meV [54], the latter being from a recent study. Our theoretical value differs by less than 10 meV from this measurement. Only a limited number of BSE studies exist for bulk  $\text{MoS}_2$ . A commonly cited reference (Ref. 55) reports an exciton binding energy of 130 meV, significantly higher than our value. This discrepancy arises from the coarse  $12 \times 12 \times 3$   $\mathbf{k}$ -point set used in that study. Indeed, our calculated value of 134 meV for the same mesh is in very good agreement with theirs.

The second and third columns show the dimension of the full electron-hole Hamiltonian and the symmetry-reduced effective block, which is about one sixth of the dimension of the Hamiltonian, corresponding to a 216-fold speedup of the diagonalization.

Figure 8 shows a graphical representation of the exciton binding energies as a function of the  $\mathbf{k}$ -point sampling  $n \times n \times 3$ . As in the case of Si, the convergence curves

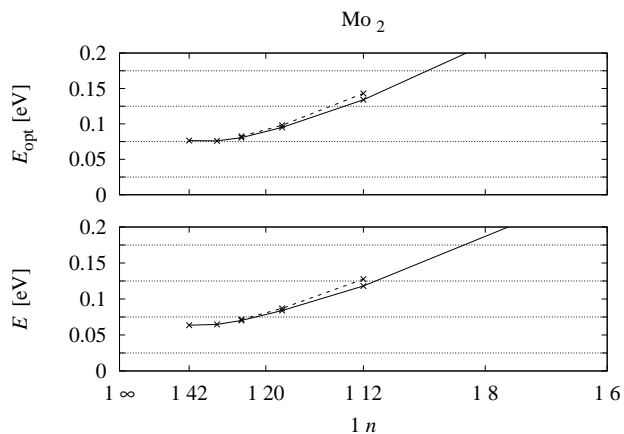


FIG. 8. Same as Fig. 2 for bulk MoS<sub>2</sub>. The solid (dashed) line refers to the  $\mathbf{k}$ -point sampling  $n \times n \times 3$  ( $n \times n \times 5$ ).

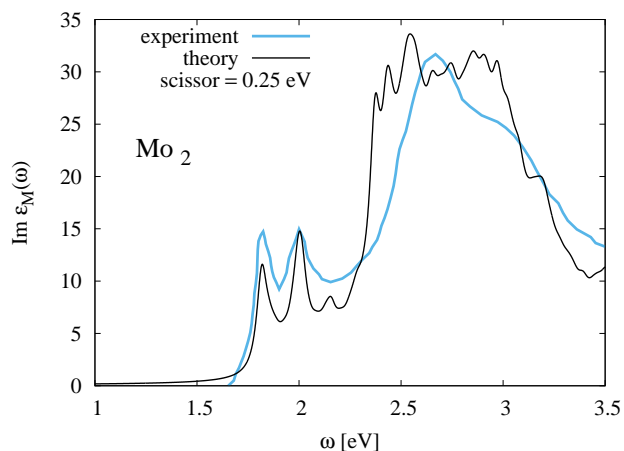


FIG. 9. Comparison of the theoretical ( $42 \times 42 \times 3$ ) and experimental absorption spectrum [56] for bulk MoS<sub>2</sub>.

flatten at the densest  $\mathbf{k}$ -point mesh of  $42 \times 42 \times 3$ , indicating that the corresponding value should be close to the infinite-mesh limit. We also included  $E_{\text{opt}}$  and  $E_b$  values calculated with the denser out-of-plane sampling  $n \times n \times 5$ , shown as dashed lines. The two curves are very close to each other, in particular, towards denser in-plane  $\mathbf{k}$ -point meshes, demonstrating that the out-of-plane sampling with three momenta is sufficient.

Finally, Fig. 9 compares the theoretical optical absorption spectrum, computed using a  $42 \times 42 \times 3$   $\mathbf{k}$ -point mesh, with the experimental spectrum reported in Ref. 56. The theoretical spectrum is scissor-shifted by 0.25 eV. The typical double-peak structure at the onset of the spectrum consisting of excitons A and B is well reproduced. The peak of exciton A is slightly smaller than that of exciton B in the theoretical spectrum, whereas in the experiment the two peaks have approximately the same height. Between 2.4 eV and 3.1 eV, both spectra exhibit a broad feature with a similar intensity of more than twice that of excitons A and B. In the experiment, this feature appears somewhat narrower than in the theoretical

spectrum. Additionally, a small peak is visible in the theoretical spectrum between this broad feature and exciton B, which is absent in the experimental data. However, an earlier experimental study [Ref. 52] does report a faint feature in this region.

## V. SUMMARY

In this paper, we described our implementation of the Bethe-Salpeter equation approach for calculating optical absorption and electron-energy loss spectra within the all-electron full-potential linearized augmented-plane-wave (FLAPW) method. To represent the bare and screened Coulomb interaction potentials, we employ the mixed basis, which is derived from the LAPW basis and adapted to represent products of wavefunctions.

It was demonstrated how crystal symmetries can be exploited to accelerate the construction and diagonalization of the electron-hole Hamiltonian in the Bethe-Salpeter equation. Only a small number of interaction matrix elements (both exchange and direct terms) need to be computed explicitly; all others can be generated by applying symmetry transformations to these elements. Moreover, transforming the conventional electron-hole product basis to a symmetry-adapted product basis using a projection operator from group theory brings the Hamiltonian into a sparse, block-diagonal form, one block per irreducible representation (irrep). For the systems considered in this study, only one of the blocks turns out to contribute to the optical absorption spectrum. The other blocks do not contribute because the oscillator strengths of their corresponding eigenstates vanish due to symmetry. As a result, the dimension of the electron-hole Hamiltonian for bulk silicon is reduced by a factor of five, leading to a 125-fold speedup in the diagonalization step. In the case of bulk MoS<sub>2</sub>, this speedup even reaches a factor of 216.

We also showed how the divergence of the screened Coulomb interaction at the point  $\mathbf{k} = \mathbf{0}$  can be treated accurately, including the case of anisotropic screening described by a non-diagonal dielectric tensor. Among the systems studied in this work, bulk MoS<sub>2</sub> is an example of a material with such a non-diagonal dielectric tensor. Once a set of eigensolutions is available for the optical absorption spectrum, determining the corresponding set of eigensolutions for the electron-energy loss spectrum requires only negligible additional computational effort.

Due to the large size of the electron-hole Hamiltonian, simulations of big systems or calculations with dense  $\mathbf{k}$ -point meshes require the matrix to be distributed across multiple compute nodes. We therefore developed efficient parallel algorithms (1) to distribute the Hamiltonian matrix elements – whose computation is non-contiguous due to the exploitation of crystal symmetries – across compute nodes and (2) to transform the electron-hole Hamiltonian into a symmetry-adapted basis and, at the same time, distribute the matrix into a block-cyclic layout

across the processes, suitable for the application of diagonalization routines from ScaLAPACK or ELPA.

The speedup achieved by the usage of symmetry enabled BSE calculations for Si to be converged to a very fine  $\mathbf{k}$ -point set of  $60 \times 60 \times 60$  using a product basis band cutoff of  $n_{\text{occ}} n_{\text{unocc}} = 5.6$  (see Sec. IV). The resulting optical absorption spectrum closely reproduces the experimental lineshape and yields an exciton binding energy of 22.5 meV, in better agreement with the experimental value of 14 meV than in previous BSE studies. Similarly good agreement is obtained for LiF. The optical absorption spectrum of MoS<sub>2</sub> was calculated including spin-orbit coupling, yielding the characteristic double-peak structure at the onset of the spectrum. The calculated exciton binding energy of 76 meV is significantly closer to the experimental value of  $\sim 85$  meV than in pre-

vious BSE studies. The most demanding calculation involved an electron-hole Hamiltonian with a dimension of nearly two million for LiF.

## ACKNOWLEDGMENTS

We thank Dmitrii Nabok, Francesco Sottile, and Matteo Gatti for fruitful discussions. Computing time on the supercomputer JURECA [57] at Forschungszentrum Jülich provided under the grants Topomag and cjiff13 is gratefully acknowledged. This work was supported by the European Centre of Excellence MaX “Materials design at the Exascale” (Grant No. 824143).

---

\* c.friedrich@fz-juelich.de

- [1] L. Hedin, *Phys. Rev.* **139**, A796 (1965).
- [2] G. Onida, L. Reining, R. W. Godby, R. Del Sole, and W. Andreoni, *Phys. Rev. Lett.* **75**, 818 (1995).
- [3] M. Rohlfing and S. G. Louie, *Phys. Rev. Lett.* **81**, 2312 (1998).
- [4] G. Onida, L. Reining, and A. Rubio, *Rev. Mod. Phys.* **74**, 601 (2002).
- [5] J. Enkovaara, C. Rostgaard, J. J. Mortensen, J. Chen, M. Dulak, L. Ferrighi, J. Gavnholt, C. Glinsvad, V. Haikola, H. A. Hansen, H. H. Kristoffersen, M. Kuisma, A. H. Larsen, L. Lehtovaara, M. Ljungberg, O. Lopez-Acevedo, P. G. Moses, J. Ojanen, T. Olsen, V. Petzold, N. A. Romero, J. Stausholm-Møller, M. Strange, G. A. Tritsarlis, M. Vanin, M. Walter, B. Hammer, H. Häkkinen, G. K. H. Madsen, R. M. Nieminen, J. K. Nørskov, M. Puska, T. T. Rantala, J. Schiøtz, K. S. Thygesen, and K. W. Jacobsen, *Journal of Physics: Condensed Matter* **22**, 253202 (2010).
- [6] A. Marini, C. Hogan, M. Grüning, and D. Varsano, *Computer Physics Communications* **180**, 1392 (2009).
- [7] M. Giantomassi, M. Stankovski, R. Shaltaf, M. Grüning, F. Bruneval, P. Rinke, and G.-M. Rignanese, *phys. stat. sol. (b)* **248**, 275 (2011).
- [8] M. Rohlfing and S. G. Louie, *Phys. Rev. B* **62**, 4927 (2000).
- [9] C. Friedrich, A. Schindlmayr, S. Blügel, and T. Kotani, *Phys. Rev. B* **74**, 045104 (2006).
- [10] P. Puschnig and C. Ambrosch-Draxl, *Phys. Rev. B* **66**, 165105 (2002).
- [11] R. Laskowski and N. E. Christensen, *Phys. Rev. B* **74**, 075203 (2006).
- [12] C. Vorwerk, B. Aurich, C. Cocchi, and C. Draxl, *Electronic Structure* **1**, 037001 (2019).
- [13] D. Pashov, S. Acharya, W. R. Lambrecht, J. Jackson, K. D. Belashchenko, A. Chantis, F. Jamet, and M. van Schilfgaarde, *Computer Physics Communications* **249**, 107065 (2020).
- [14] R. Zhou, Y. Yao, V. Blum, X. Ren, and Y. Kanai, *Journal of Chemical Theory and Computation* **21**, 291 (2025).
- [15] T. Kotani and M. van Schilfgaarde, *Solid State Communications* **121**, 461 (2002).
- [16] C. Friedrich, S. Blügel, and A. Schindlmayr, *Phys. Rev. B* **81**, 125102 (2010).
- [17] M. Betzinger, C. Friedrich, S. Blügel, and A. Göring, *Phys. Rev. B* **83**, 045105 (2011).
- [18] M. Betzinger, C. Friedrich, and S. Blügel, *Phys. Rev. B* **81**, 195117 (2010).
- [19] I. M. Alliati, D. Sangalli, and M. Grüning, *Frontiers in Chemistry* **9**, 763946 (2022).
- [20] S. Blügel and G. Bihlmayer, “Full-potential linearized augmented planewave method,” in *Computational Nanoscience: Do It Yourself!*, NIC Series, Vol. 31, edited by J. Grotendorst, S. Blügel, and D. Marx (John von Neumann Institute for Computing, 2006) p. 85–122.
- [21] J. Stöhler, *Implementation of the Bethe-Salpeter Equation for Absorption Spectroscopy within the FLAPW Method*, Master’s thesis, RWTH Aachen University (2021), masterarbeit, RWTH Aachen University, 2021.
- [22] S. L. Adler, *Phys. Rev.* **126**, 413 (1962).
- [23] N. Wiser, *Phys. Rev.* **129**, 62 (1963).
- [24] O. K. Andersen, *Phys. Rev. B* **12**, 3060 (1975).
- [25] D. D. Koelling and G. O. Arbman, *Journal of Physics F: Metal Physics* **5**, 2041 (1975).
- [26] E. Wimmer, H. Krakauer, M. Weinert, and A. J. Freeman, *Phys. Rev. B* **24**, 864 (1981).
- [27] D. Singh, *Phys. Rev. B* **43**, 6388 (1991).
- [28] C. Friedrich, A. Schindlmayr, and S. Blügel, *Computer Physics Communications* **180**, 347 (2009).
- [29] C. Friedrich, S. Blügel, and A. Schindlmayr, *Phys. Rev. B* **104**, 039901 (2021).
- [30] S. Massidda, M. Posternak, and A. Baldereschi, *Phys. Rev. B* **48**, 5058 (1993).
- [31] To be precise, there is the relation  $|S| = \sum_{\mu} d_{\mu}^2$  with the number of symmetry operations  $|S|$  and the dimension  $d_{\mu}$  (1, 2, or 3) of the  $\mu$ th irrep. The sum runs over all irreps.
- [32] Our criterion for the basis transformation was the block-diagonality of  $\Gamma$ . This still permits any two matrix representations, say  $\Gamma_m$  and  $\Gamma_{m'}$ , to be formally different but equivalent; that is, there exists a unitary matrix  $U$  such that  $\Gamma_m(s) = U^{-1} \Gamma_{m'}(s) U$  for all  $s$ . In other words, they are in the same equivalence class. It is then straightforward to incorporate  $U$  into the basis transformation to

- make  $\Gamma_m$  and  $\Gamma_{m'}$  identical.
- [33] M. I. Aroyo, A. Kirov, C. Capillas, J. M. Perez-Mato, and H. Wondratschek, *Acta crystallographica. Section A, Foundations of crystallography* **62 Pt 2**, 115 (2006).
- [34] IUCr, *International Tables for Crystallography, Volume A: Space Group Symmetry*, 5th ed., edited by T. Hahn (Kluwer Academic Publishers, Dordrecht, Boston, London, 2002).
- [35] P. H. Hahn, K. Seino, W. G. Schmidt, J. Furthmüller, and F. Bechstedt, *physica status solidi (b)* **242**, 2720 (2005).
- [36] M. Grüning, A. Marini, and X. Gonze, *Computational Materials Science* **50**, 2148 (2011).
- [37] S. Rost, S. Blügel, and C. Friedrich, *Phys. Rev. B* **107**, 085132 (2023).
- [38] J. Choi, J. Demmel, I. Dhillon, J. Dongarra, S. Ostrouchov, A. Petitet, K. Stanley, D. Walker, and R. C. Whaley, in *Applied Parallel Computing Computations in Physics, Chemistry and Engineering Science*, edited by J. Dongarra, K. Madsen, and J. Waśniewski (Springer Berlin Heidelberg, Berlin, Heidelberg, 1996) pp. 95–106.
- [39] T. Auckenthaler, V. Blum, H.-J. Bungartz, T. Huckle, R. Johanni, L. Krämer, B. Lang, H. Lederer, and P. Willems, *Parallel Computing* **37**, 783 (2011), 6th International Workshop on Parallel Matrix Algorithms and Applications (PMAA'10).
- [40] A. Marek, V. Blum, R. Johanni, V. Havu, B. Lang, T. Auckenthaler, A. Heinecke, H.-J. Bungartz, and H. Lederer, *Journal of Physics: Condensed Matter* **26**, 213201 (2014).
- [41] J. P. Perdew, K. Burke, and M. Ernzerhof, *Phys. Rev. Lett.* **77**, 3865 (1996).
- [42] H. R. Philipp and E. A. Taft, *Phys. Rev.* **120**, 37 (1960).
- [43] M. A. Green, *AIP Advances* **3**, 112104 (2013).
- [44] J. Sun, J. Yang, and C. A. Ullrich, *Phys. Rev. Res.* **2**, 013091 (2020).
- [45] A. M. Alvertis, A. Champagne, M. Del Ben, F. H. da Jornada, D. Y. Qiu, M. R. Filip, and J. B. Neaton, *Phys. Rev. B* **108**, 235117 (2023).
- [46] P. Lautenschlager, M. Garriga, L. Vina, and M. Cardona, *Phys. Rev. B* **36**, 4821 (1987).
- [47] M. Piacentini, *Solid State Communications* **17**, 697 (1975).
- [48] M. Piacentini, D. W. Lynch, and C. G. Olson, *Phys. Rev. B* **13**, 5530 (1976).
- [49] N.-P. Wang, M. Rohlfing, P. Krüger, and J. Pollmann, *Phys. Rev. B* **67**, 115111 (2003).
- [50] T. Deilmann, *Phys. Rev. B* **98**, 165105 (2018).
- [51] D. M. Roessler and W. C. Walker, *J. Opt. Soc. Am.* **57**, 835 (1967).
- [52] A. R. Beal, J. C. Knights, and W. Y. Liang, *Journal of Physics C: Solid State Physics* **5**, 3540 (1972).
- [53] E. Fortin and F. Raga, *Phys. Rev. B* **11**, 905 (1975).
- [54] N. Saigal, V. Sugunakar, and S. Ghosh, *Applied Physics Letters* **108**, 132105 (2016).
- [55] H.-P. Komsa and A. V. Krasheninnikov, *Phys. Rev. B* **86**, 241201 (2012).
- [56] A. R. Beal and H. P. Hughes, *Journal of Physics C: Solid State Physics* **12**, 881 (1979).
- [57] Jülich Supercomputing Centre, *Journal of large-scale research facilities* **7** (2021), 10.17815/jlsrf-7-182.